JGR Solid Earth

RESEARCH ARTICLE
10.1029/2022JB025353

Spatio-Temporal Evolution of Aftershock and Repeater Source Properties After the 2016 Pedernales Earthquake (Ecuador)

Caroline Chalumeau[1], Hans Agurto-Detzel[2], Louis De Barros[1], Philippe Charvis[1], and the Rapid Response Team of the 2016 Pedernales Earthquake[3]

[1]Université Côte d'Azur, IRD, CNRS, Observatoire de la Côte d'Azur, UMR Géoazur, Valbonne, France, [2]Geophysical Institute (GPI), Karlsruhe Institute of Technology, Karlsruhe, Germany, [3]See Appendix A

Abstract Subduction zones are highly heterogeneous regions capable of hosting large earthquakes. To better constrain the processes at depth, we analyze the source properties of 1514 aftershocks of the 16th April 2016 M_w 7.8 Pedernales earthquake (Ecuador) using spectral ratios. We are able to retrieve accurate seismic moments, stress drops, and *P* and *S* corner frequencies for 341 aftershocks, including 136 events belonging to families of repeating earthquakes. We find that, for the studied magnitude range (M_w 2–4), stress drops appear to increase as a function of seismic moment. They are also found to depend on their distance to the trench. This is in part explained by the increase in depth, and therefore normal stress, away from the trench. However, even accounting for the shallow depths of earthquakes, stress drops appear to be anomalously low near the trench, which can be explained by a high pore fluid pressure or by inherent properties of the medium (low coefficient of friction/low rigidity of the medium) in that region. We are also able to examine the temporal evolution of source properties thanks to the presence of repeating earthquakes. We find that the variations of source properties within repeating earthquake families are not uniform, and are highly spatially variable over most of the study area. This is not the case near the trench, however, where stress drops systematically decrease over time. We suggest that this reflects an increase in pore fluid pressure near the trench over the postseismic period.

Plain Language Summary Recovering earthquake source size and magnitude can provide valuable insight into the state of stress and friction on a fault. Of particular importance is the stress drop, the difference in static stress on the asperity before and after the earthquake. The stress drops and source sizes of small earthquakes can be affected by nearby large earthquakes. Here, we examine the source properties of 341 aftershocks of the 16th April 2016, M_w 7.8 Pedernales earthquake that occurred at the Ecuadorian subduction zone. We find that the stress drops of aftershocks tend to increase with magnitude, which implies that earthquakes source properties are scale-dependant. We also find that stress drops are anomalously low near the trench, which may be due to the presence of fluids or to different properties (lower rigidity/friction coefficient) in the region. With the help of repeating earthquakes, which rupture the same asperity at different times, we are able to determine how earthquake source properties evolve over time. When looking at the evolution of source properties in time, we find that unlike in most of the region, stress drops decrease with time near the trench. This may reflect an increase in the pore fluid pressure over time in that region.

Key Points:

- Source properties of 341 aftershocks of the Mw 7.8 2016 Pedernales earthquake (Ecuador) are recovered
- Stress drops appear to increase with seismic moment in the region
- We find low and decreasing stress drops near the trench, possibly indicative of high pore fluid pressure

Supporting Information:

Supporting Information may be found in the online version of this article.

Correspondence to:

C. Chalumeau,
caroline.chalumeau@kit.edu

Citation:

Chalumeau, C., Agurto-Detzel, H., De Barros, L., Charvis, P., & the Rapid Response Team of the 2016 Pedernales Earthquake (2023). Spatio-temporal evolution of aftershock and repeater source properties after the 2016 Pedernales earthquake (Ecuador). *Journal of Geophysical Research: Solid Earth*, *128*, e2022JB025353. https://doi.org/10.1029/2022JB025353

Received 5 AUG 2022
Accepted 28 JAN 2023

Author Contributions:

Conceptualization: Caroline Chalumeau
Formal analysis: Caroline Chalumeau, Hans Agurto-Detzel, Louis De Barros, Philippe Charvis
Funding acquisition: Philippe Charvis
Methodology: Caroline Chalumeau, Hans Agurto-Detzel, Louis De Barros
Project Administration: Philippe Charvis
Software: Caroline Chalumeau, Hans Agurto-Detzel
Supervision: Hans Agurto-Detzel, Louis De Barros, Philippe Charvis
Visualization: Caroline Chalumeau
Writing – original draft: Caroline Chalumeau

1. Introduction

Subduction zones are home to some of the largest and most potentially damaging earthquakes on Earth. These regions often present a complex slip behavior, as areas of slow aseismic slip can neighbor earthquake rupture. The slip behavior is strongly controlled by the geometry, the structural heterogeneity and the stress state of the megathrust. To know whether a large and damaging earthquake can occur on a given portion of a fault, we therefore need to characterize the fault properties and processes acting upon it in detail. Characterizing the source physics of small to moderate earthquakes can allow us to gain key insights into the large-scale mechanical properties of a fault. In particular, stress drop ($\Delta\sigma$) indicates the difference in stress levels between the start and end of an earthquake, and can therefore be an indicator of the initial stress heterogeneities on the fault, as well as its shear strength.

On average, stress drop is thought to be constant across scales (Abercrombie, 1995; Aki, 1967; Allmann & Shearer, 2009). However, in detail, variations in stress drops have been observed and linked to a variety of factors. Some studies have found an increase in stress drops with magnitudes on regional scales (Bindi et al., 2020),

Writing – review & editing: Caroline Chalumeau, Hans Agurto-Detzel, Louis De Barros, Philippe Charvis

and other studies have found that stress drops increase with magnitude but plateau at high magnitudes (Drouet et al., 2011). This remains a controversial point, as observed trends may result from errors in stress drop calculations (Abercrombie, 2021). Tectonic setting can also affect stress drops, as intraplate earthquakes in stable regions typically have higher stress drops than interplate earthquakes (Viegas et al., 2010). Similarly, faulting type seems to influence stress drops, as some studies show strike-slip earthquakes tend to have higher stress drops (Allmann & Shearer, 2009), although other studies found that thrust faulting earthquakes have higher stress drops than strike-slip ones at depth (Hardebeck & Aron, 2009).

Some authors have found a degree of correlation between stress drops of microearthquakes and the coseismic slip areas of large earthquakes: stress drops were sometimes found to be high around past rupture zones and low within them (Yamada et al., 2021), although that correlation is ambiguous (Allmann & Shearer, 2007; Shearer et al., 2006). Similarly, Hardebeck and Aron (2009) found that stress drops of earthquakes in and around locked zones were higher on average than those on creeping portions of the Hayward fault (California) at similar depths, suggesting a link to coupling. Stress drops have also sometimes been found to increase with depth in the crust as a consequence of the increase in vertical stress (Boyd et al., 2017; Hardebeck & Aron, 2009; Huang et al., 2017), including in subduction zones (Oth, 2013; Uchide et al., 2014). Stress drops depending primarily on applied shear stress is consistent with both their increase with depth and their relationship to fault locking and faulting type (Hardebeck & Aron, 2009). Finally, pore fluid pressure can decrease stress drops and rupture velocity, as has been shown experimentally (Passelègue et al., 2020) and observed for induced (X. Chen & Shearer, 2011; Goertz-Allmann et al., 2011; Kwiatek et al., 2014) and natural earthquakes (Yoshida et al., 2017).

Variations of stress drops with time have also been observed, especially after large earthquakes. However, there is no unique behavior expected after a mainshock, as both increases and decreases in stress drop have been observed (X. Chen & Shearer, 2013). Shear stress changes induced by the mainshock may account for some of the observed changes in stress drop after a large earthquake (Allmann & Shearer, 2007).

When studying temporal variations in source properties, repeating earthquakes are ideal tools, as they are thought to represent the repeated rupture of a single asperity due to loading from surrounding aseismic slip (Ellsworth, 1995). They can therefore be used as proxy to study the temporal evolution of the frictional properties of the fault (Vidale et al., 1994). Large earthquakes greatly impact repeating earthquakes, causing a significant decrease followed by an increase in recurrence times, as well as a change in seismic moment that can be positive or negative, and sometimes the emergence of new repeating families (T. Chen & Lapusta, 2009; K. H. Chen et al., 2010; Hatakeyama et al., 2017; Peng et al., 2005). Some rupture processes of repeating earthquakes are remarkably similar, maintaining a consistent rupture direction and velocity and occasionally a consistent stress drop (Abercrombie et al., 2012). In other cases, repeating earthquake stress drops have decreased and gradually recovered after a large earthquake (Abercrombie, 2014; Chaves et al., 2020). This has been explained by the decrease in healing time after a large earthquake leading to a decrease in static coefficient of friction on neighboring asperities (Abercrombie, 2014; Chaves et al., 2020; Scholz, 1998).

In this paper, we use both repeating and non-repeating aftershocks to understand the spatial and temporal variability of source properties in the aftermath of a large megathrust earthquake. Our study focuses on the postseismic period of the Mw 7.8 2016 Pedernales earthquake in Ecuador (Figure 1). The Pedernales earthquake occurred in a region of varying interseismic coupling that hosts both large earthquakes and slow slip events. It was the fifth event above magnitude 7.5 that occurred in the region since 1900. The first and largest was the Mw 8.4–8.8 1906 event (Kanamori & McNally, 1982; Yoshimoto et al., 2017), which ruptured a 200–500 km-long portion of the Ecuador-Colombia subduction zone (Kelleher, 1972). Three other Mw 7.7–8.2 earthquakes occurred in the 20th century, all within the 1906 rupture zone. The 1942 earthquake ruptured its southern portion, the 1958 earthquake ruptured its middle portion and the 1979 earthquake ruptured its northern portion. The Pedernales earthquake broke the highly coupled southern segment, similar to the 1942 earthquake (Chlieh et al., 2014; Nocquet et al., 2014, 2017). It may have released all of the strain stored since 1942 (Ye et al., 2016; Yoshimoto et al., 2017), or may have released more strain than what was accumulated since 1942, thus hinting at the existence of an earthquake supercycle and explaining the apparent quiescence of the Ecuador-Colombia subduction zone before 1906 (Nocquet et al., 2017).

Aseismic slip controls a large portion of the seismicity in the region, as was highlighted in the aftermath of the Pedernales earthquake. In the month following the mainshock, the aftershock expansion and moment release were controlled primarily by the afterslip (Agurto-Detzel et al., 2019). The seismicity was arranged into three

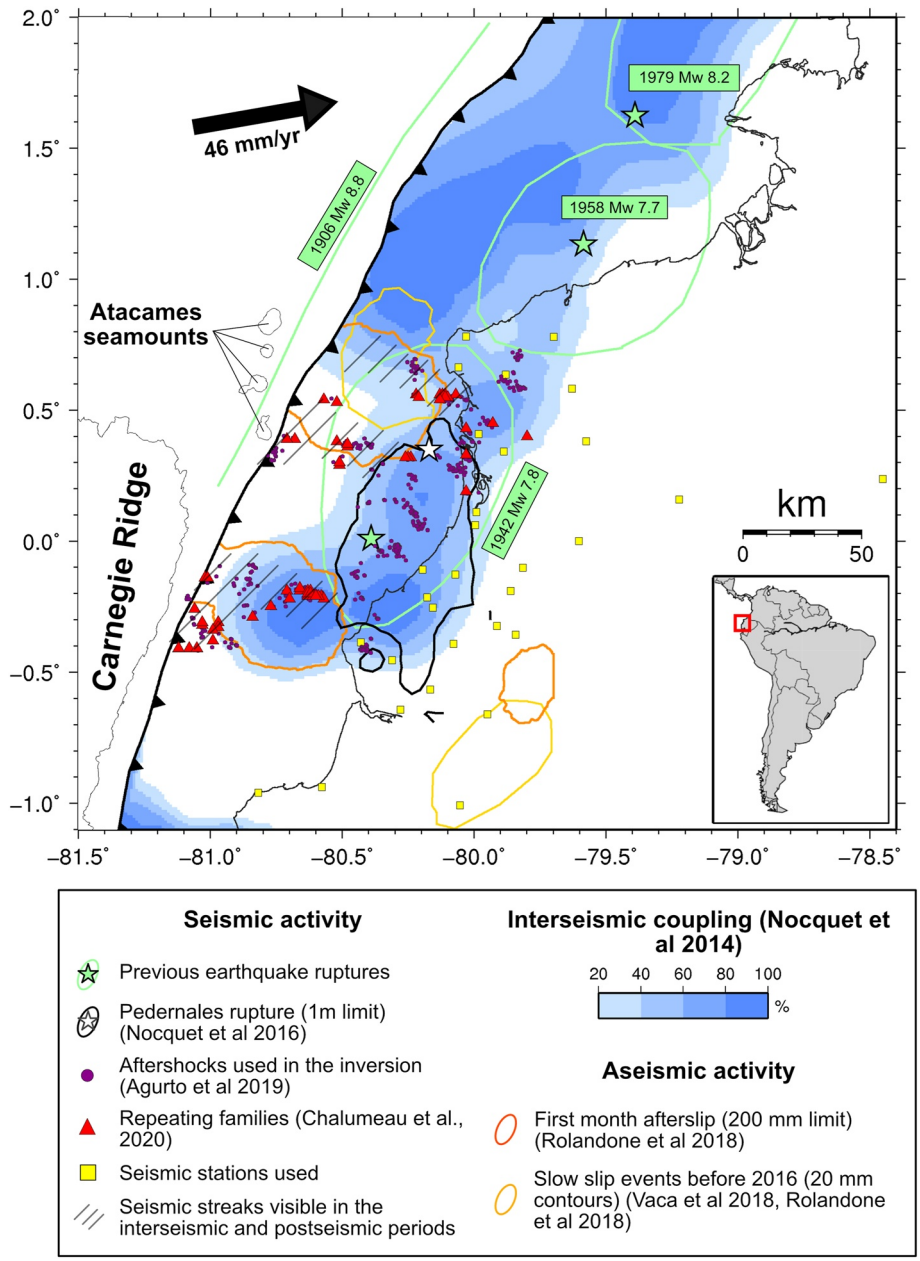

Figure 1. Seismotectonic features of the study region. The main bathymetric features of the incoming plate are labeled, along with the plate convergence rate between the Nazca plate and the North Andean Sliver from Chlieh et al. (2014). Stars show the epicenters of the Pedernales earthquake (in white) and previous megathrust earthquakes (in green). The green circles show the rough outlines of past megathrust earthquakes (Kanamori & McNally, 1982; Mendoza & Dewey, 1984) while the black line shows the geodetically derived rupture zone of the 2016 Pedernales earthquake (Nocquet et al., 2017). The orange lines show the 20 cm edges of the Pedernales afterslip during the first month (Rolandone et al., 2018). Yellow lines show the 20 mm edges of geodetically observed slow slip events occurring prior to 2016 (Rolandone et al., 2018; Vaca et al., 2018). The dark red circles show the locations of all 1514 events used in this study, while the triangles show the locations of the 62 repeating earthquake families. The hatched areas show the approximate location of the three streaks of seismicity described by Font et al. (2013).

streaks going from the rupture zone to the trench, which are permanent features of the background seismicity (Font et al., 2013). These streaks contained a large number of repeating earthquakes, which occurred primarily at the edge of the two afterslip patches (Chalumeau et al., 2021). These patterns of seismicity are likely controlled primarily by the subducting features on the Nazca plate, although variations in upper plate composition and structure has also been found to possibly control megathrust rupture extent (Koch et al., 2020; Lynner

et al., 2020). The subducting Atacames seamounts likely participate in reducing the interseismic coupling and may act as barriers preventing large ruptures from propagating up-dip (Marcaillou et al., 2016). Meanwhile, to the south, the Carnegie Ridge, a 2 km high, 280 km wide, and 14–19 km thick volcanic feature, subducting between 0° and 2.5°S, likely limits rupture propagation in this direction (Collot et al., 2004; Gailler et al., 2007; Graindorge et al., 2004; Michaud et al., 2009; Sallarès et al., 2005).

In this context, we explore not only what features control the spatial distribution of microearthquakes' stress drops, but also the evolution of their source properties in the aftermath of a large subduction earthquake. Through this, we hope to better understand the evolution of the frictional properties of the megathrust, and the recovery process after the mainshock. For this purpose, we use the spectral ratios method to recover seismic moments, corner frequencies and stress drops of both repeaters and regular aftershocks of the Pedernales earthquake. We find that stress drops increase with moment magnitude. Furthermore, we note that earthquakes near the trench have on average lower and decreasing stress drops. Elsewhere, stress drops remain highly heterogeneous, with no clear pattern of evolution.

2. Materials and Methods

2.1. Earthquake and Station Selection

We examine 14 months of postseismic data of the Pedernales earthquake, using both the permanent Ecuadorian seismic network (Alvarado et al., 2018), as well as the temporary seismic stations deployed for 1 year after the Pedernales earthquake (Agurto-Detzel et al., 2019; Meltzer et al., 2019). We use the aftershock catalog published by Agurto-Detzel et al. (2019) using both automatic and manual detections and located with a 1D model (Figure 2). Within this catalog, 2,925 events were partially relocated with both NonLinLoc (Lomax et al., 2000) and HypoDD (Waldhauser & Ellsworth, 2000) by Chalumeau et al. (2021). 1514 of these events are sorted into 55 clusters of seven or more earthquakes with a maximum distance of 9 km, corresponding to twice the average absolute location error for our relocated earthquakes (Chalumeau et al., 2021). We use these earthquakes for our inversion. As for repeating earthquakes, we use the catalog of 376 repeaters sorted into 62 families of 4–15 events detected by Chalumeau et al. (2021) (Figures 1 and 2). This catalog was constructed using cross-correlation with a threshold of 0.95, and was completed using template-matching to ensure the completeness of families.

To infer source properties, we use the spectral ratios method, also known as the multiple empirical Green's function (meGf) method, developed by Ide et al. (2003) and based on an approach by Hough (1997), to obtain seismic moments and corner frequencies. This method works as follows. A seismogram can be written as $S(t) = E(t) * G(t) * I(t)$ where E is earthquake source, G is propagation (Green's function) and I is instrument response, which we know. According to the Boatwright spectral model (Boatwright, 1980), the source displacement spectrum is given by: $E(f) = \left(\frac{\Omega}{1+(f/f_c)^{\gamma n}}\right)^{\frac{1}{\gamma}}$, where Ω is the low-frequency asymptote, f_c the corner frequency and γ and n are two constants assumed to be $\gamma = 2$ and $n = 2$. Meanwhile, G is unknown. However, for two closely located events, the path from event to station, and therefore G, should be the same. So by taking a ratio of the two events at the same station in the frequency domain, we can remove propagation effects and be left with only the source information:

$$\frac{S_1(f)}{S_2(f)} = \frac{M_{01}}{M_{02}}\left(\frac{1+(f/f_{c2})^{\gamma n}}{1+(f/f_{c1})^{\gamma n}}\right)^{\frac{1}{\gamma}} \quad (1)$$

Often, this method is used to recover the source properties of one large event using one or several much smaller events as empirical Green's functions. However, this requires large magnitude differences between collocated events, which we do not have in several places. We instead elect to invert the ratios of all suitable earthquake pairs within a cluster together, using only a small minimum magnitude difference of 0.1 (Text S3 and Figure S14 in Supporting Information S1). This approach is similar to that taken by Lengliné et al. (2014) and Agurto-detzel et al. (2017).

We use 30 stations with sampling rates of 100, 125, or 200 Hz. These stations (Figure S1 in Supporting Information S1) are chosen based on their quality, their azimuthal coverage and their availability. However, even with these precautions, the first and last months, which fall outside the temporary deployment (Meltzer et al., 2019),

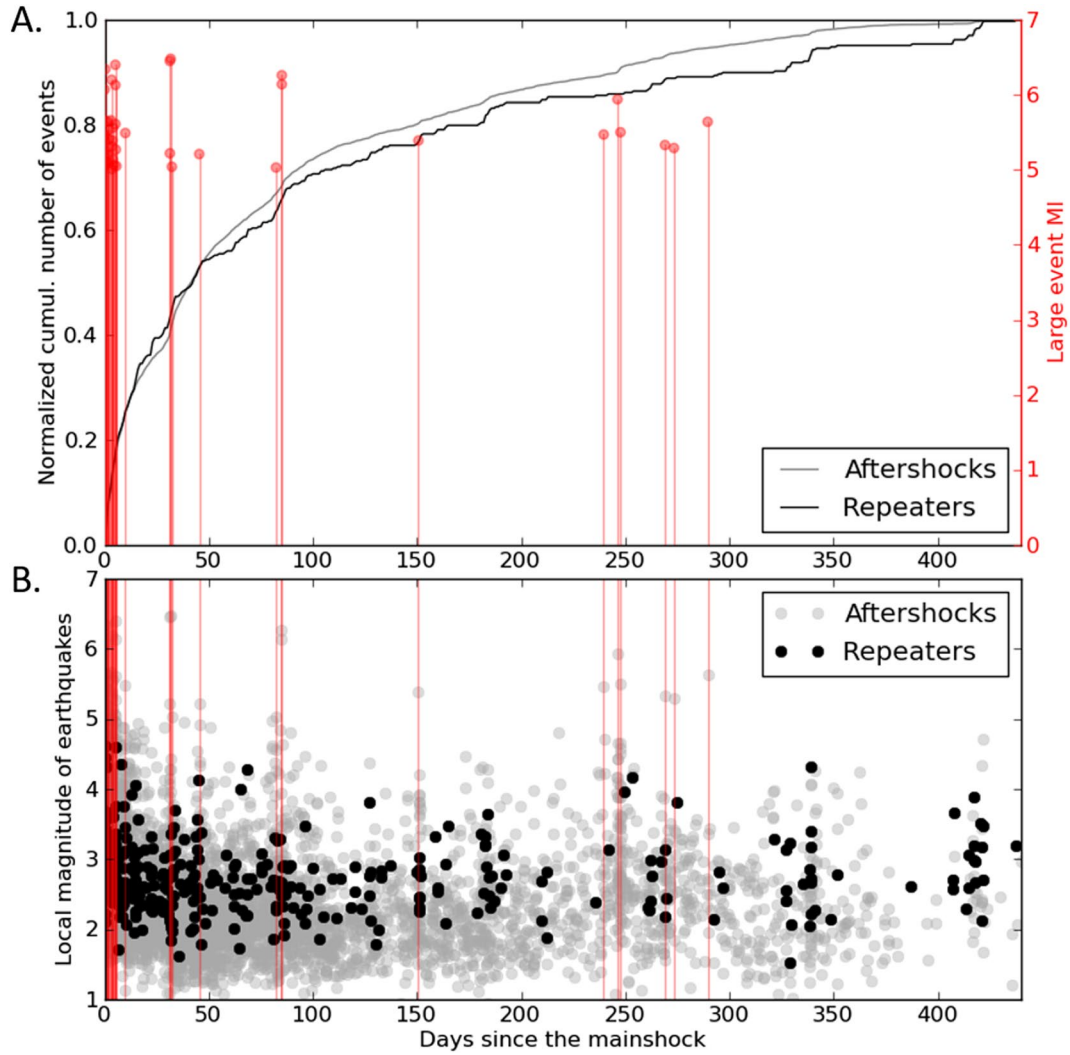

Figure 2. Time and magnitude of earthquakes in the initial catalog. In gray are aftershocks from the Agurto-Detzel et al. (2019) catalog, and in black are the repeaters from the Chalumeau et al. (2021) catalog. The red lines and circles are the large-magnitude earthquakes with local magnitudes above 5. (a) Cumulative number of aftershocks and repeaters as a function of time, normalized by the total number of aftershocks and repeaters. (b) Local magnitudes of aftershocks and repeaters as a function of time.

have significantly fewer stations available, which makes events during that time less well constrained. At all times however, at least 7 stations are present.

2.2. Spectral Analysis

We separate the *P* and *S* waves throughout the whole process, as stations are far enough that the two phases are usually distinct. Within a single cluster and for a given station, we keep the lengths of *P* and *S* time windows constant as 0.6 * $(Ts–Tp)_{average}$ and 1.2 * $(Ts–Tp)_{average}$ respectively, starting 0.1 s before the *P* and *S* arrivals. To avoid contamination from one phase to another, and to account for errors in theoretical arrivals, we discard any window smaller than 2 s, and any cluster-station pair with $(Ts–Tp)_{average}$ smaller than 2.5 s. Using these time windows, we calculate *P* spectra on the vertical component and *S* spectra on the horizontal ones using the multitaper code developed by Prieto et al. (2009). An example of *S* wave spectra for repeating earthquake families is shown in Figure 3. Noise spectra are also calculated using the same window lengths but ending 2 s before the *P* arrival. These spectra are smoothed and resampled in log space to ensure that higher frequencies do not weigh more than lower ones in the inversion.

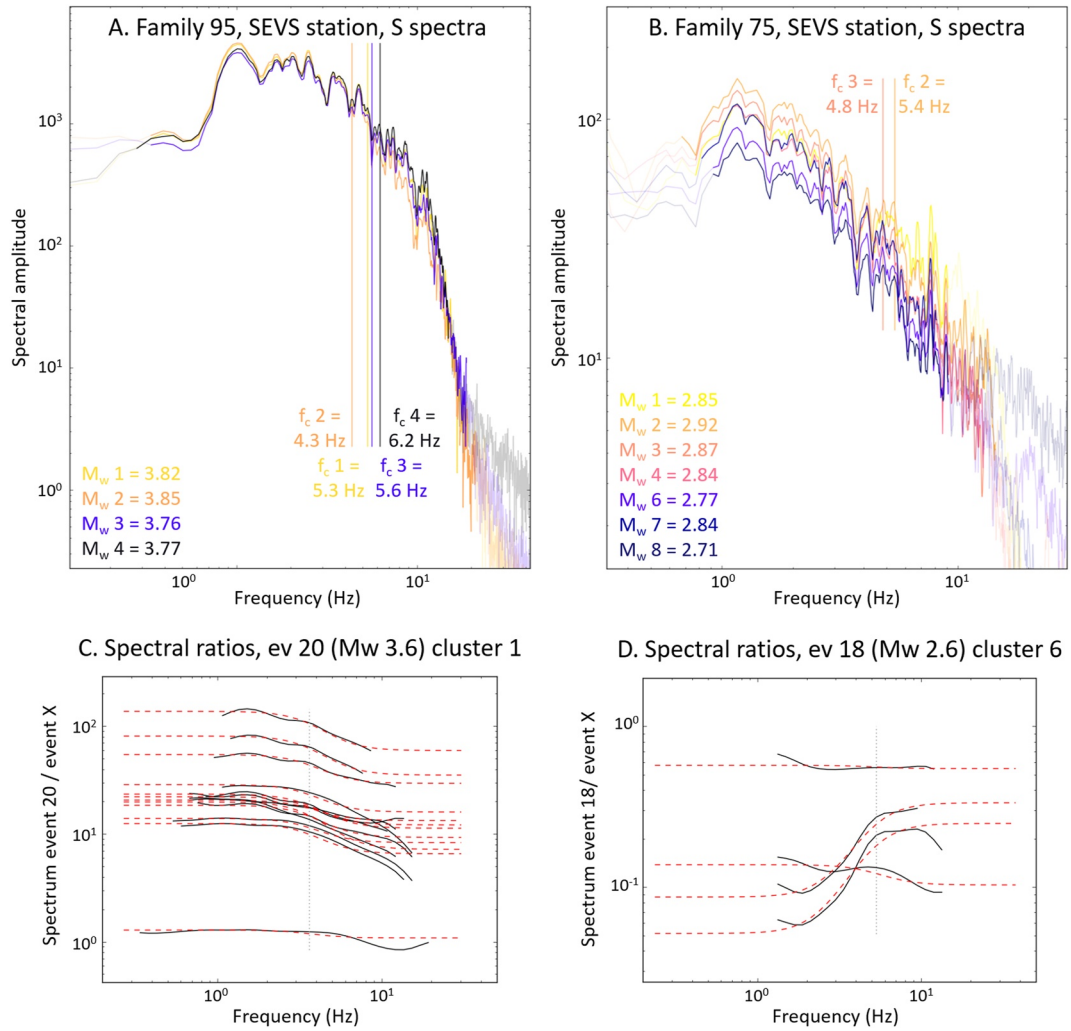

Figure 3. Examples of spectra and spectral ratios. (a) *S* velocity spectra of repeating earthquakes in family 95 at SEVS station, calculated in a 17-s window. Faded lines are areas of the spectrum that are excluded from spectral ratio modeling as $S/N < 4$. The line color refers to the event number within the family, with yellow and black showing the first and the last event, respectively. Vertical lines show the computed corner frequencies. (b) Same as a, for a family of repeating events (family 75) near the trench, using a 20.2 s window at SEVS station. (c) Spectral ratios used to calculate source properties for the *S* phase of event 20 in cluster 1 with SEVS station. Full black lines are the real spectral ratios (calculated where $S/N > 4$) and dashed red lines are the modeled spectral ratios. The dotted gray line is the event's corner frequency. (d) Same as c for event 18 in cluster 6, at SEVS station.

Before the inversion, we use the displacement spectra of each earthquake to calculate preliminary seismic moments. We fit this general model to the part of the spectrum where $S/N >= 3$, using the equation:

$$D(f) = \frac{\Omega e^{-\pi f t/Q}}{\left(1 + (f/f_c)^{\gamma n}\right)^{\frac{1}{\gamma}}} \quad (2)$$

Where t is the phase travel time and Q is the frequency-independent quality factor, left free in the inversion but around 700 on average for the P wave and 900 for the S wave over the whole region. Using the modeled Ω, we calculate seismic moment as $M_0 = \frac{4\pi\rho c^3 r\Omega}{U}$ (Shearer, 2009) where ρ is density, c is phase velocity, r is the event-station distance and U is the radiation pattern, which depends on the focal mechanism but can be averaged to 0.52 for P waves and 0.63 for S waves (Boore & Boatwright, 1984). These values of M_0 are later used as starting values for the inversion, with corresponding starting corner frequencies calculated by assuming a 2 MPa stress drop.

Before calculating spectral ratios, correlation coefficients are computed in the time domain between event seismograms within a cluster. An event pair is used in the final inversion at a given station if it has a correlation coefficient above 0.8 at more than 90% of stations where correlations can be calculated and at the station examined. Having high correlation coefficients like this ensures that the events are collocated, which in turn is necessary to obtain accurate results (Abercrombie, 2015).

In order to minimize any unnecessary manipulation of data, we elect not to convert our data to displacement when calculating spectral ratios. The spectral ratios are only computed over the part of the spectrum where $S/N >= 4$, on the condition that log(fmax)–log(fmin) >= 0.7. This higher signal-to-noise ratio helps ensure that noise does not influence our moments and especially our corner frequencies.

Before inverting for all corner frequencies and seismic moments, each individual spectral ratio is modeled, and those that are poorly fit by Equation 1 or that yield unrealistic results are discarded (fc below 0.1 or above 100 or M_0 below 10^6 or above 10^{20}). We also discard spectral ratios when both corner frequencies fall well outside the frequency range of the data.

Finally, we invert all remaining spectral ratios for a cluster at a single station together. In order to constrain the absolute values of seismic moment, we use the logarithmic mean of the preliminary seismic moments, which is kept constant during the inversion. We run the inversion several times with different starting M_0 and fc, and keep the results with the smallest numerical error. If the inversion cannot converge, we remove problematic events. We show an example of inverted spectral ratios in Figure 3. We take an event's seismic moment and corner frequency to be the median between available stations. From seismic moments, we calculate moment magnitudes using the equation by Hanks and Kanamori (1979):

$$M_w = 2/3\left(\log_{10}(M_0) - 9.1\right) \tag{3}$$

We also calculate static stress drops as:

$$\Delta\sigma = \frac{7}{16}\left(\frac{f_c}{k v_s}\right)^3 M_0 \tag{4}$$

From Eshelby (1957) and Brune (1970). Here v_s is the S wave velocity, given as 2,900 m/s, the average S wave velocity at our earthquakes' depth (Agurto-Detzel et al., 2019). k is a constant which differs between P and S and depends on rupture velocity (Kaneko & Shearer, 2014). As discussed later, we set k_P as 0.33 and k_S as 0.26. This model assumes that the rupture is circular, and therefore that any change in fc is due to a change in size of the rupture. The event stress drop is taken to be the logarithmic mean of the P and S stress drop.

2.3. Uncertainties

We calculate uncertainties by performing a jackknife test on our data (Agurto-detzel et al., 2017; Prieto et al., 2007). For each cluster and each station, we run 100 inversions where we resample the spectral ratio data, removing 20% of data points within spectral ratios. We estimate the error as the standard deviation of the logarithms of seismic moments, corner frequencies, and stress drops obtained. For this study, we only keep events which have errors below $10^{0.5}$ for stress drop, $10^{0.2}$ for fcP, $10^{0.2}$ for fcS and 0.2 for Mw.

Since every ratio has its own frequency range of analysis, there are no frequency limits common to all earthquakes beyond which corner frequencies cannot be resolved. However, we determine that corner frequencies that exceed half of the maximum frequency at which a ratio is calculated are underestimated, and therefore discarded (Text S1 and Figure S5 in Supporting Information S1). We do however keep the estimation of magnitude from these earthquakes, since it relies on low-frequency signal.

Finally, we ensure that the use of earthquakes from different times after the mainshock, hence with possible medium velocity and attenuation variations, does not significantly bias our results (Text S2 and Figure S13 in Supporting Information S1).

3. Results

3.1. Source Properties Within the General Population of Earthquakes

Out of 1514 aftershocks examined, we recover the source properties of 582 events using P waves, and 584 events using S waves, of which 341 events have both P and S source properties. Due to the uneven station coverage,

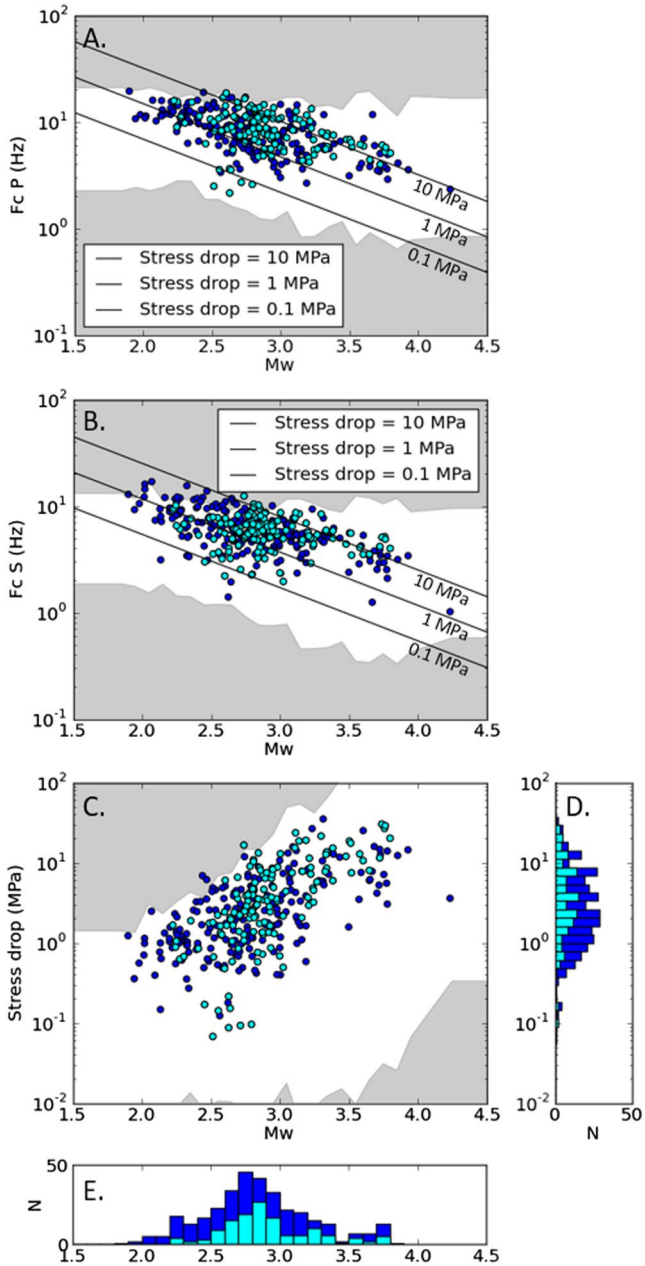

Figure 4. Panels (a)–(c) show source properties (corner frequencies inferred from *P*-waves and *S*-waves, stress drop) as a function of moment magnitude. Panels (d and e) show the distribution of stress drops and magnitudes respectively. Light blue represents repeaters and dark blue represents non-repeaters. The gray shaded areas show for a given magnitude the median upper and lower frequency limits between which corner frequencies can be resolved.

first month events are more likely to be missing. Corner frequency, moment magnitude and stress drop distributions are shown in Figure 4. About 90% of corner frequencies are within 4–15 Hz for the *P* wave and 3–11 Hz for the *S* wave, with median values of 8 and 6 Hz respectively.

The median *P*/*S* corner frequency ratio is 1.27 (Figure S3 in Supporting Information S1). This ratio appears to be constant with corner frequency, stress drop and magnitude (Figure 5). Since $f_c = kv_s/L$ (Brune, 1970), where k is a constant linked to the rupture process, the *P*/*S* corner frequency ratio must be equal to k_P/k_S. According to Kaneko and Shearer (2014), k_P, k_S, and k_P/k_S are affected by the rupture velocity and the geometry of the rupture (Kaneko & Shearer, 2015). Since rupture geometries are likely very diverse at such a large scale, the average k_P/k_S ratio probably reflects the average velocity of rupture. A ratio of 1.27 corresponds to a rupture velocity of about 0.75 v_s, so we set k_P as 0.33 and k_S as 0.26 (Kaneko & Shearer, 2014) to compute the stress drops (4). Other studies have found similar v_r/v_s based on *P*/*S* corner frequency ratios in subduction zones (Yamada et al., 2021). Note however that this ratio is an average in space and time, and therefore the scattering can be explained by varying rupture velocities and geometries among events.

Our moment magnitudes vary between 2.2 and 3.8 with a median of 2.8, while stress drops are mostly log-normally distributed and vary between 0.4 and 15 MPa with a median of 2.5 MPa (Figures 4d and 4e). This is within the expected range for a subduction zone (Abercrombie et al., 2017; Oth et al., 2010; Yoshida et al., 2017). Overall, while repeaters tend to have higher magnitudes than non-repeaters, they generally seem to have the same magnitude-stress drop distribution as non-repeaters at this scale. For both repeaters and non-repeaters, we see an increase of stress drop with moment magnitude (Figure 4c). This could be a result of selection bias, since corner frequencies above half of the high frequency bandwidth limit were discarded, or it could reflect a real change in source properties with magnitude. In Figures 4a–4c, shaded areas represent frequencies below the median lower frequency limit and above half of the median upper frequency limit. These areas are lacking events, as earthquakes falling within them are more likely to have unresolvable corner frequencies.

The catalog's moment magnitude of completeness is 2.6 (Figure S2 in Supporting Information S1, Agurto-Detzel et al., 2019). If there is an increase of stress drops with magnitude beyond our sampling bias, then it must be possible above that magnitude for the 472 events that were discarded during the inversion to fully compensate the observed trend, assuming stress drops to be log-normally distributed at every magnitude range (Allmann & Shearer, 2009). While the distribution of stress drops in the lower magnitude range appears truncated (Figure S6 in Supporting Information S1), there are too few discarded events to explain our observed increase of stress drops with magnitude while assuming that the average stress drop remains above 9.6 MPa (as it is for events with magnitudes above 3.5).

Our corner frequency estimates may also be biased. When modeling spectral ratios, if one of the corner frequencies is too close to the edge of the bandwidth, allowing that corner frequency as a free parameter may contaminate the corner frequency estimation of the other event (Shearer et al., 2019). We ensure this is not the cause of our trend by inverting for the spectral ratios of low-corner frequency events, while assuming a corner frequency corresponding to a stress drop of 2 MPa for all the high frequency events. Doing so does not remove the trend, meaning the increase in stress drops with magnitudes is likely real (Figure S7 in Supporting Information S1).

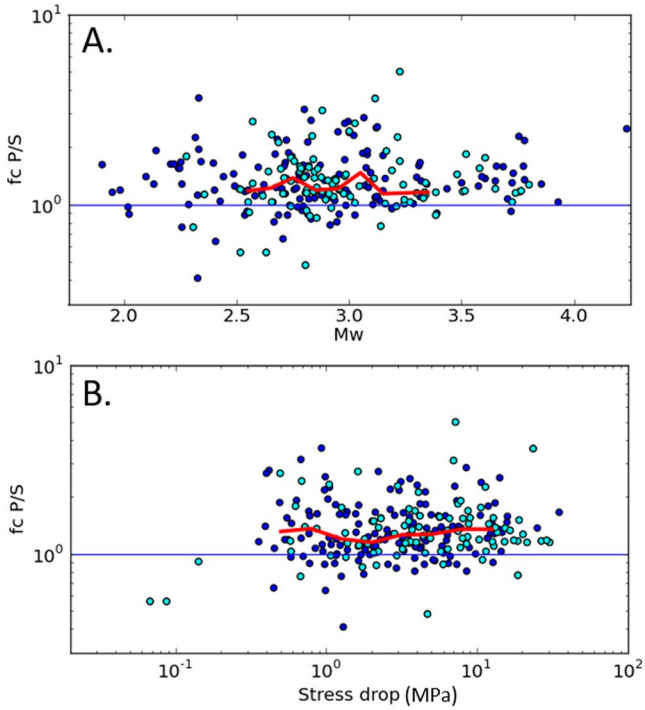

Figure 5. *P*/*S* corner frequency ratio as a function of *M*w (a) and stress drop (b). Light blue represents repeaters and dark blue represents non-repeaters. The red line is the median.

Thus since stress drop most probably increases with magnitude for our catalog, we investigate the cause of this increase. Both location and timing could affect magnitudes and stress drops, and could therefore be creating this trend. However, when coloring earthquakes with respect to time (Figure 6a), we see that early and late earthquakes have the same trend and have similar stress drops in the high magnitudes, although there are fewer low-magnitude earthquakes in the first month of aftershocks due to fewer stations being available, making the detection threshold higher. Therefore, timing is unlikely to explain the magnitude versus stress drop trend. Event location, particularly depth, is another candidate to explain this relationship. Because depth itself is poorly resolved, particularly near the trench, we consider distance from the trench as a general proxy for depth, assuming earthquake hypocenters are close to the plate interface. We see that distance to the trench has an impact on the Mw versus stress drop relationship (Figure 6b). Events 20 km or under from the trench stand apart, with lower stress drops and a steeper trend. Events in the 20–60 km group have the same trend but lower stress drops compared to events in the >60 km group. However, for all three groups, we see that stress drops increase with magnitudes. Therefore, although distance to the trench influences stress drop, it cannot explain why stress drops increase with magnitude.

The dependence of stress drops on magnitudes, combined to the spatially variable magnitude of completeness, means that the dependence of stress drops on depth is complex to see in map view (Figure 7a). However, we do see that stress drops are clearly lower near the trench, especially in the south where stress drops increase from the trench to the transition between the rupture zone and the southern afterslip patch. On average, the median stress drop is observed to increase with depth (Figure 7c). This increase with depth is not linked to an increase of magnitudes (Figure 7b), in part because the magnitude of completeness near the trench is much higher. A slight variation of stress drop is also observed with the coupling (Figure 7d). However, as the coupling is globally increasing away from the trench, this variation is likely attributable to depth. The distance to the trench is also inversely correlated to the average event-station distance, which could mean that the attenuation linked to distance may contribute to low stress drop measurements near the trench (Figure S15 in Supporting Information S1). However, we find that it cannot fully account for the low observed stress drops near the trench (Text S4 and Figures S16 and S17 in Supporting Information S1).

Away from the trench, stress drops do not show large anomalies or any significant variations with the afterslip areas. Stress drops might be slightly lower within the 2016 rupture zone, although it is likely that events

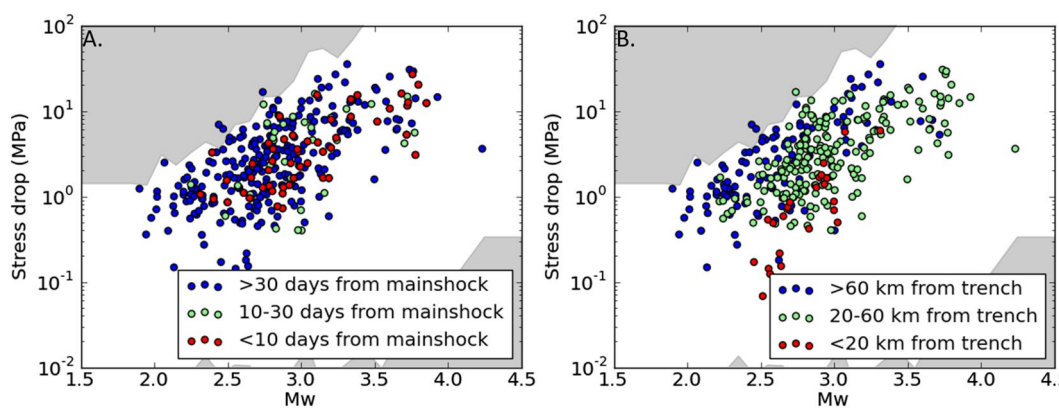

Figure 6. Distribution of stress drops as a function of magnitude. (a) Events colored by time. The timing of repeaters does not influence the stress drop Versus magnitude trend. (b) Events colored by distance to the trench. The gray shaded areas show for a given magnitude the median upper and lower frequency limits between which corner frequencies can be resolved.

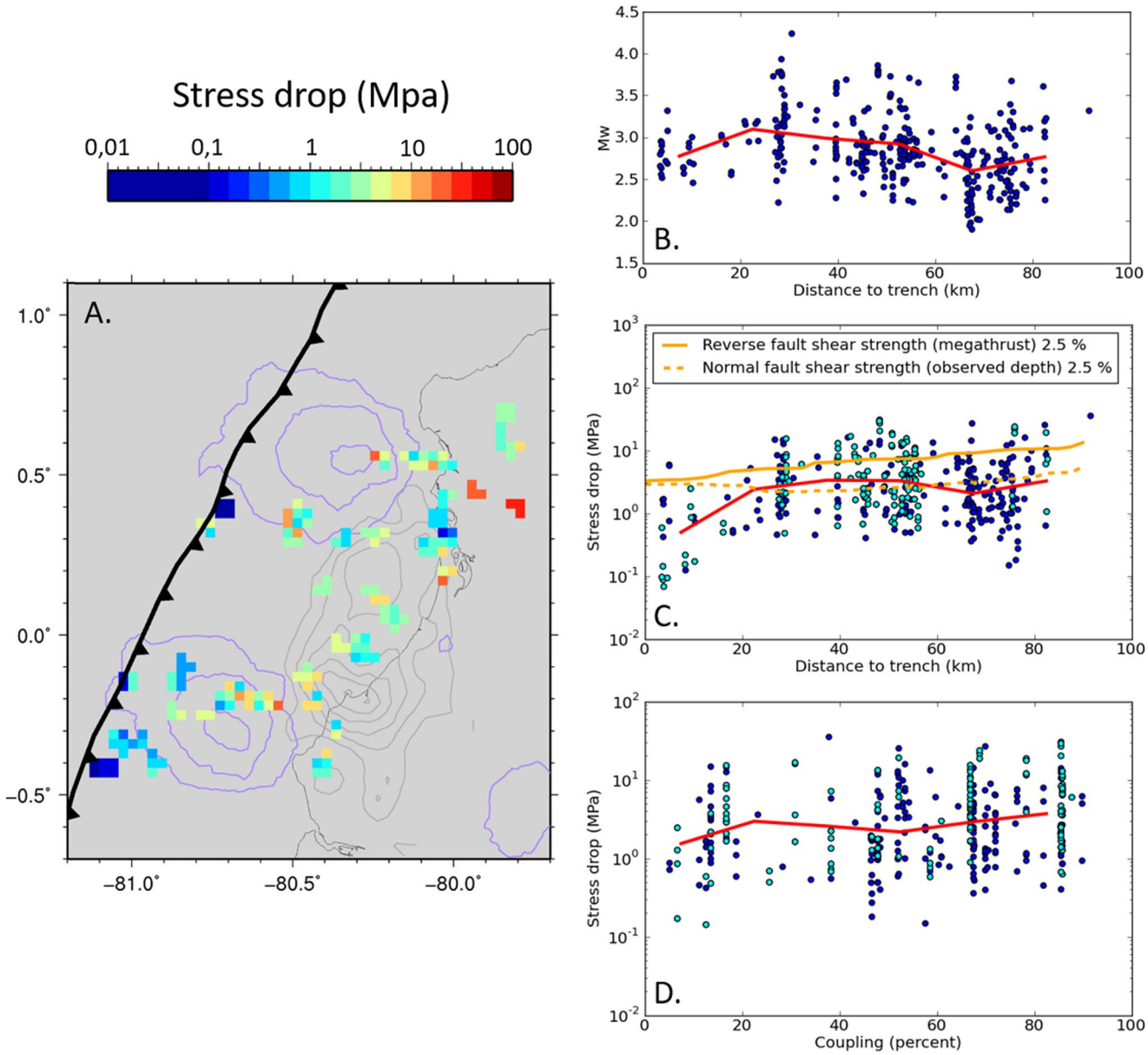

Figure 7. Spatial distribution of stress drop. (a) shows a map of all stress drops calculated, with colors representing their logarithm. The purple lines are the 20 cm contours of the afterslip (Rolandone et al., 2018), while the gray lines are the 1 m contours of the Pedernales rupture (Nocquet et al., 2017). (b) Shows the magnitude of events with full source properties as a function of distance to the trench. (c) Shows stress drop as a function of distance from the trench, with the orange lines showing the expected shear strength based on earthquake depth, and the depth of the interface (Hayes et al., 2012). (d) shows the relationship of stress drops to coupling. In b, c, and d, the red line is the median.

in that area occur distributed within the seismogenic volume, making comparisons to interplate earthquakes difficult (Agurto-Detzel et al., 2019). What we mainly see is significant spatial variability in stress drops, even among very close events, meaning that local heterogeneities likely control stress drops. Such spatial variability has already been documented in other regions, including subduction zones (Abercrombie et al., 2017; Baltay et al., 2013).

Thus, stress drops appear highly heterogeneous in space and show a dependency on depth and magnitudes. In order to fully characterize the evolution of source properties with time, we look at changes at a single location within repeating earthquake families.

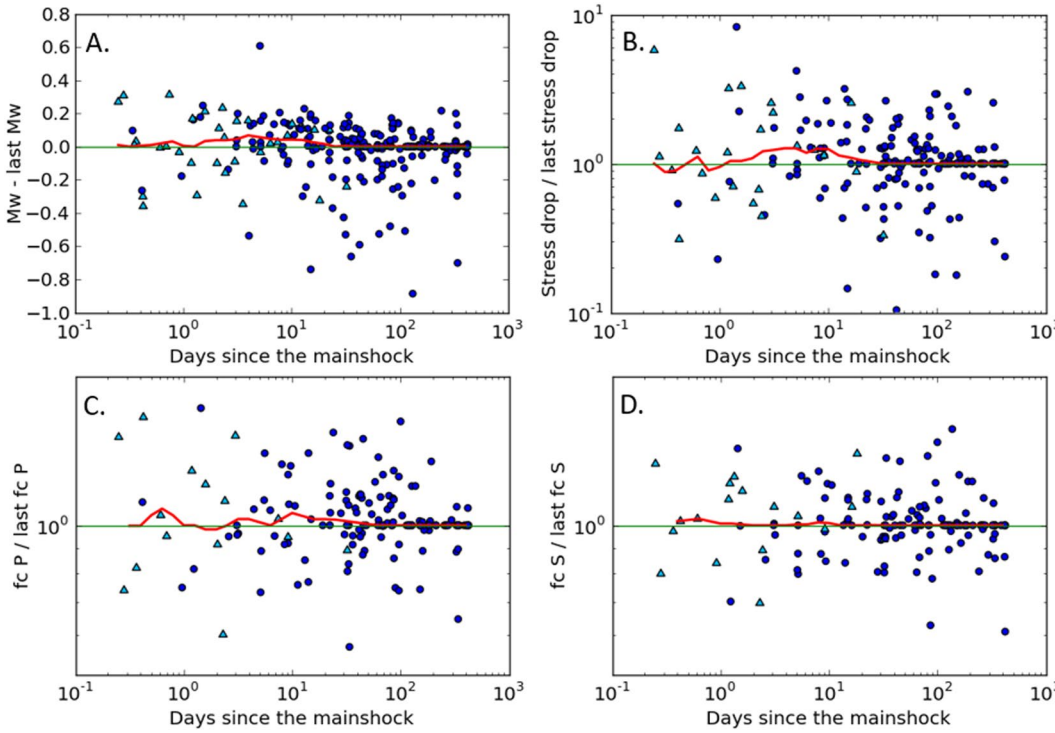

Figure 8. Evolution of normalized source properties within families. Panel (a) shows moment magnitude differences, panel (b) normalized stress drops, and panels (c and d) normalized *P* and *S* corner frequencies. Each event within a family is normalized by the last event of that family with all source properties determined. The red line is the median computed using a sliding window of 1 in log space. Triangles represent the first event after the mainshock within a family.

3.2. Source Properties Within Families of Repeaters

Out of the 376 repeaters identified by Chalumeau et al. (2021), we recover *P* and *S* source properties from 136 events. Missing events are due to a combination of low station availability, low signal-to-noise ratio, and a lack of nearby events with distinct magnitudes and corner frequencies. We look for global trends in the evolution of source properties in time by normalizing each family of repeaters by the source properties of its last fully recovered event, which should be the closest to the background response (Figure 8). We also show source properties as a function of recurrence times in Figure S12 in Supporting Information S1, but because in most cases recurrence times increase with time (Chalumeau et al., 2021), there are no significant differences between these two analyses. For all events, we normalize properties station by station, to limit the impact of our evolving network on the results. Seismic moment appears high right after the mainshock and decreases with time, while corner frequencies remain on average constant but very scattered (Figure 8). Consequently, stress drops are also very scattered but tend to decrease with time, like the moment magnitude. Overall, the large scatter in these plots indicates that families exhibit many different behaviors.

Out of the 62 families of repeaters, 34 have at least 3 magnitudes and 3 stress drops calculated, or have more than 5 magnitudes. We show their individual evolutions over time in Figure S9 of the Supporting Information S1. Overall, *P* and *S* corner frequencies usually change together and demonstrate a wide variety of behavior. Corner frequencies increase with time in 4 families, decrease in 6, and are stable in 10. Additionally, there are cases where the evolution of corner frequencies is more complicated, as well as cases where the number of resolved corner frequencies within the family is too low to have a reliable trend. Meanwhile, out of the 26 families with visible trends in Mw with time, 5 have increasing Mw while 18 have decreasing Mw, confirming that there is less variability in the changes of magnitudes with time. Consequently, the stress drops increase with time for 3 families and decrease with time for 15 families with visible trends, while it remains stable for 3 families.

Overall, families that are very close can have very different stress drops and different time variations of stress drops. We do however see regional patterns in the time evolution of source properties in the region near the trench

(Figure S8 in Supporting Information S1). In this area, all 6 families with resolvable stress drop changes see a decrease in stress drop throughout the whole period, and all 5 out of 6 families with distinct trends in moment magnitude also have decreasing moments, while one (family 100) has an initial increase followed by a decrease. An example of S wave spectrum for one family in the region is shown as an example in Figure 3, where the difference in moment is immediately evident. Many families in this region have corner frequencies that are difficult to resolve. Nevertheless, provided that we assume that P and S corner frequencies behave similarly, then corner frequencies are either stable or decrease in the region. This might reflect a measurement bias due to an increase in attenuation over time. Using a similar method to Kelly et al. (2013) and assuming that all repeaters within a family have the same stress drop, then we have:

$$\ln\frac{S_1(f)}{S_2(f)} = \ln\frac{M_{01}}{M_{02}} + \ln\left(\left(\frac{1+(f/f_{c2})^{\gamma n}}{1+(f/f_{c1})^{\gamma n}}\right)^{\frac{1}{\gamma}}\right) + \left(\frac{t}{Q_2} - \frac{t}{Q_1}\right)\pi f \tag{5}$$

Where t is the travel time and Q is the quality factor along the path to the station. For a given family, we fit all spectral ratios with this equation, assuming a constant stress drop (Figure S10 in Supporting Information S1). We find that the data can be fit with such an equation, proving that it is possible for attenuation to explain our results in the region provided there is an increase in both corner frequencies and attenuation over time. In the 200 days after the mainshock, the difference in $\frac{1}{Q}$ between the first and the last repeater is between -0.0005 and -0.001 (Figure S11 in Supporting Information S1). No absolute estimates of Q exist for the near-trench region in Ecuador. However, assuming a Q of 50–100, as is found near the Hikurangi trench (Nakai et al., 2021), our $\frac{1}{Q}$ changes correspond to an increase in attenuation of 1.5%–10% over the first 200 days of the postseismic period. This is despite the fact that damage from the earthquake and gradual fault healing should induce a high attenuation after the mainshock, that decreases over time.

4. Discussion

Having recovered 341 stress drops within our region, we find that they are influenced primarily by magnitude and distance to the trench, with little influence from coupling or the location of slow slip. Additionally, the evolution of source properties with time on single asperities is heterogeneous, except near the trench, where stress drops are widely seen to decrease.

4.1. Relationship of Stress Drops With Magnitude

On average, the stress drops of all aftershocks appear to increase with magnitude, as observed in other parts of the world (Bindi et al., 2020). Lin and Lapusta (2018) suggest that apparent scaling of stress drop with M_0 could be due to heterogeneities on the fault. Large strength variations would lead to some portions of a fault patch not slipping, meaning the earthquake rupture would have a complex shape. Event duration, and therefore corner frequency, is controlled by the rupture length, while event magnitude depends on the rupture area. This implies that events of similar duration may have very different magnitudes, if their shape is very different. Elongated ruptures in particular can have low magnitudes but similar corner frequencies to circular ruptures if the rupture length is the same. In this way, assuming a circular rupture leads to an underestimation of the stress drop. Therefore, in some cases an apparent stress drop increase with magnitude could simply reflect a larger proportion of complex rupture shapes for low magnitudes (Lin & Lapusta, 2018). Such elongated rupture shapes would lead to lower P/S corner frequency ratios compared to what is expected from a circular rupture (Lin & Lapusta, 2018). However, we find no dependence of the P/S corner frequency ratio on either estimated stress drop or magnitude (Figure 5), leading us to conclude that rupture shape or velocity variation is not the cause of our dependence of stress drop on magnitude.

We saw in Figure 6 that the magnitude-stress drop relationship holds during different time periods, implying that it is not caused by the temporal variations of these two parameters. Therefore, the observed scaling implies that earthquakes are not self-similar within the range of magnitudes studied here. Going back to Eshelby (1957):

$$\Delta\sigma = \frac{7}{16}\frac{M_0}{R^3} \tag{6}$$

Where R is the radius of the rupture. Because we have $M_0 = \mu D A$ (Aki, 1966), where μ is the shear modulus, D is the displacement and A is the area of the rupture, having larger stress drops for larger magnitudes implies that the displacement increases faster than the size of the asperity. This increase is shown in Figure 9a, where we see

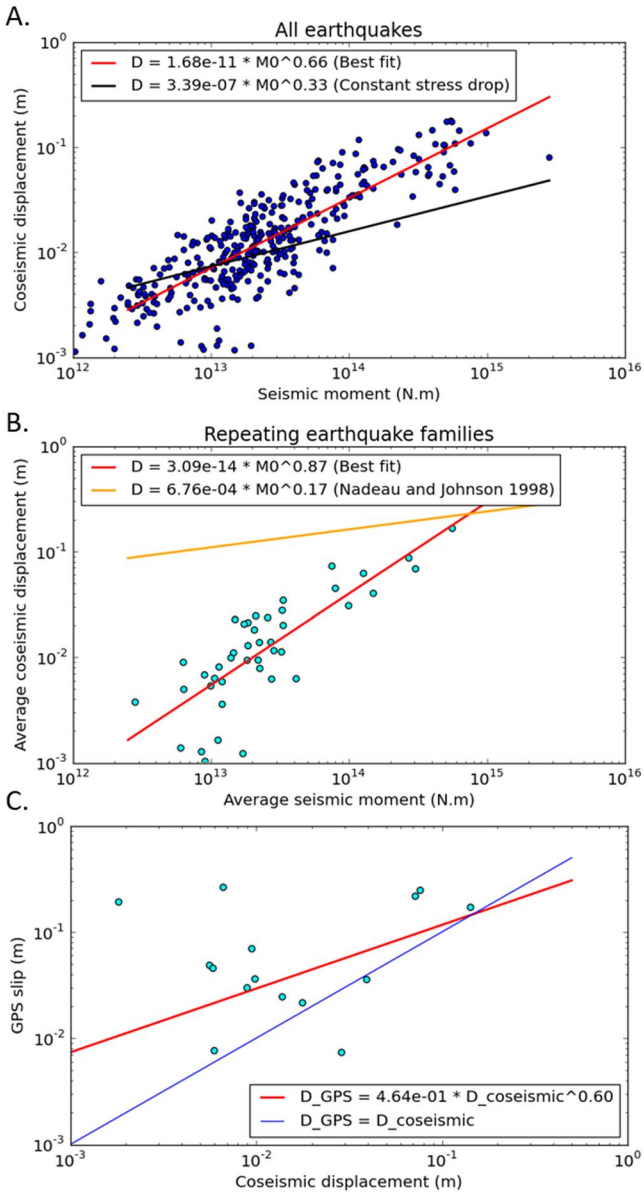

Figure 9. (a) Coseismic displacement as a function of seismic moment, for all earthquakes. The red line shows the best fit for the data, while le black line shows the theoretical increase of displacement with moment when assuming a constant stress drop of 1.9 MPa. (b) Average coseismic displacement as a function of average moment within families of repeating earthquakes. The red line is the best fit. The orange line is the relationship derived by Nadeau and Johnson (1998) using quasi-periodic repeaters on the creeping portion of the San Andreas fault. (c) Average geodetically measured slip (Rolandone et al., 2018) as a function of average coseismic displacement for families of repeating earthquakes active during the first month. The red line is the best fit, while the blue line shows the line where the GPS slip is equal to the coseismic slip.

that coseismic displacement seems to be proportional to $M_0^{2/3}$, rather than the expected $M_0^{1/3}$.

Looking specifically at repeating earthquakes in Figure 9b, we see that the relationship of seismic moment to displacement is similar for repeaters and non-repeating aftershocks. This is notable, as it is very different to the displacement predicted by the Nadeau and Johnson (1998) model. They assume that all the displacement on a repeating earthquake asperity occurs coseismically, and thus that coseismic displacement is proportional to $M_0^{1/6}$ for repeating earthquakes. This is however not verified in California, where the model was developed (Beeler et al., 2001), and we see here that this model does not hold in our context either. In fact, the GPS displacement occurring on asperities hosting repeating earthquakes seems to be almost always larger than the coseismic displacement (Figure 9c). This may be in part explained by the low resolution of slip near the trench. It may also imply, as Beeler et al. (2001) suggested, that a portion of the slip occurring on repeating earthquake asperities is aseismic. The smaller repeating earthquake asperities seem to host a higher proportion of aseismic slip than the larger asperities, which is again compatible with the model of Beeler et al. (2001). Therefore, the presence of a varying aseismic slip component in the asperity slip may explain the dependency between stress drop and moment.

4.2. Postseismic Changes in Repeating Earthquake Sources

We observe some patterns in the evolution of the source properties of repeating earthquakes with time. For many of our families of repeating events, we find that the seismic moment decays with time after the mainshock. This has been observed in several places (Chaves et al., 2020; K. H. Chen et al., 2010; Uchida et al., 2015), although lower magnitudes after a mainshock have been observed as well (K. H. Chen et al., 2010). These variations have been interpreted as a balance between two processes (Chaves et al., 2020; K. H. Chen et al., 2010; Uchida et al., 2015). On the one hand, recurrence times tend to be smaller after a mainshock, which decreases the static coefficient of friction and therefore lowers the stress drops. On the other hand, the increase in strain rate in the aftermath of the mainshock can cause transient embrittlement, which increases rupture areas and therefore lowers corner frequencies. This can occur if the nucleation length of the earthquake is initially of a similar size to the velocity-weakening patch, and is therefore more likely for smaller magnitudes (K. H. Chen et al., 2010). According to this model, if the area of slip grows sufficiently, it can compensate for the lower stress drops, and the seismic moment of the repeater increases. Otherwise, the seismic moment will be lower due to the decreased stress drop.

However, in our study area, high seismic moments after the mainshock are rarely associated with a lower corner frequency. Families tend to have constant or negative trends of corner frequency with time, which means that, when the source size does change, it is rarely larger at the start than the end of the period. Therefore, transient embrittlement is unlikely to affect most of our repeating sources and cannot account for the larger magnitudes immediately after the mainshock. On the other hand, most families have larger stress drops right after the mainshock, which then decrease with time. This refutes the idea that shorter recurrence times necessarily lead to a widespread decrease in fault strength, since our recurrence times increase with time. At the scale of individual asperities, some transient embrittlement or fault weakening may occur, but they cannot explain the general behavior of families in our data set. In fact, most regions have widespread heterogeneity with no link to large scale properties, like

slow slip or coupling, meaning that very local processes likely dictate the response of repeaters to the mainshock, with the exception of the near-trench region.

4.3. Lower Stress Drops Near the Trench

One striking observation regarding the spatial distribution of stress drops is their low values near the trench, particularly in the south, despite the higher magnitude of completeness in the region. This might indicate a dependency of stress drops with depth in our study area. Depth in this region is poorly constrained, and 3D tomography studies have located most earthquakes in this region within the subducting plate (León-ríos et al., 2021). However, most focal mechanisms that were previously calculated near the trench show thrust faulting (Agurto-Detzel et al., 2019). Thus, for simplicity in the absence of depth constraints, we cautiously assume that earthquakes in the region occur primarily near the interface. We therefore investigate the likely causes of an increase in stress drop with depth.

Previous studies have often found a dependence of stress drop (Oth, 2013) or source duration (Bilek, 2007; Bilek & Lay, 2002; Lay et al., 2012) on depth in subduction zones. Because there is a tradeoff between rupture velocity variations and stress drop variations (Lay & Bilek, 2007), our observation of low stress drops near the trench could reflect slow rupture velocities. Bilek and Lay (2002) suggested that these slow rupture velocities could be explained by the region being conditionally stable with asperities embedded in it. Slow earthquake ruptures would then be due to a large portion of the rupture propagating into the conditionally stable portion of the megathrust. However, while Tolga Şen et al. (2015) observed a decrease in normalized source duration with depth for both interplate and intraplate earthquake of Mw 4.0–6.5, they concluded that special frictional conditions near the trench were not required to explain the data. Instead, a variation of rigidity combined with an increase of stress drop with depth could well explain their observations.

We test whether the normal stress increase with depth in the Earth is enough to account for most of our observed increase in stress drop with depth, as has been the case for other studies (Huang et al., 2017). To test this, we show in Figure 7c the shear strength as a function of depth. This curve is constructed by making the same assumptions as Huang et al. (2017): a coefficient of friction of 0.6 and hydrostatic pore pressure. We show 2 separate curves: The first curve corresponds to an estimate of the shear strength for reverse faults at the plate interface, where we expect most repeaters to be. However, due to uncertainties in depth it is possible for earthquakes near the trench to be associated with normal faulting in the slab. We therefore show a second profile of shear strength for normal faulting at the average hypocentral depth. We find that stress drops follow the increase of shear strength with depth of the interface quite well between 20 and 60 km from the trench. Stress drops seem to represent around or below 2.5% of the shear strength (Figure 7c), which is predictably lower than what is found for intraplate earthquakes (Huang et al., 2017). It could mean that shear strength is overestimated, due to a fluid pressure higher than the hydrostatic one or to a friction coefficient lower than 0.6. After 60 km, stress drops are lower on average, likely because a lot of earthquakes in this region occur in the 2016 rupture zone, both at the interface and within the seismogenic volume (Agurto-Detzel et al., 2019). At this distance, repeating earthquakes, which occur outside of the Pedernales rupture zone and likely on the interface, have higher stress drops, comparable to what we expect if stress drop increases with depth. Meanwhile, within 20 km of the trench, stress drops span a wider range, but are on average too low to be explained by the lower strength caused by the shallower depth. This is true even if we only consider events recorded at least 75 km from the source, thus removing the effect of event-station distance on the stress drop trend (Figure S17 in Supporting Information S1). This means that the low values of stress drop near the trench are due to conditions specific to that region, be they a higher pore fluid pressure, a lower coefficient of friction or a lower rigidity of the medium.

The thinned and highly fractured upper lithosphere imaged by Marcaillou et al. (2016) where the Atacames seamounts enter subduction may help explain why the stress drops in that region would be low. It may significantly alter the stiffness of the medium, and possibly the friction. Marcaillou et al. (2016) also finds that the subduction channel between the subducted seamounts is likely filled with overpressurized fluids, which may also contribute to the low stress drops. The presence of a large volume of fluids near the trench is confirmed by seismic tomography studies, which finds a low vp and high vp/vs ratio in this region (León-ríos et al., 2021). High pore fluid pressure has been found to lower stress drops, and thus could play a role here (Goertz-Allmann et al., 2011; Passelègue et al., 2020; Yoshida et al., 2017).

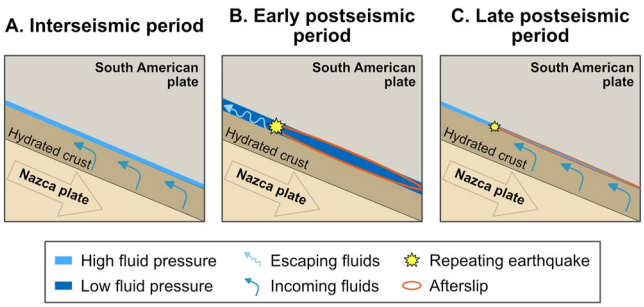

Figure 10. Schematic diagram of the evolution of pore fluid pressure near the trench during the postseismic period. (a) Interseismic period: fluid pressure is high as fluids are trapped at the plate interface. (b) Early postseismic period: fluid pressure is low as afterslip causes dilation and fluids escape the interface. (c) Late postseismic period: fluid pressure increases again as the afterslip slows down.

Another possibility is that of afterslip playing a role in lowering stress drops. GPS studies show that some slip occurs near the trench (Rolandone et al., 2018; Tsang et al., 2019), and a high slip rate can lower the static coefficient of friction, leading to smaller stress drops (K. H. Chen et al., 2010). There are two factors that prevent us from considering this as the main cause of low stress drops near the trench. The first is that other regions further inland appear to be experiencing higher slip rates during the postseismic period (Figure 7; Rolandone et al., 2018; Tsang et al., 2019), and yet they have higher stress drops on average. The other issue is that repeating earthquakes' stress drops in the region appear to decrease as recurrence time increases, which implies that slip rate is not the main factor controlling stress drops in the region. We therefore suggest that the low stress drops near the trench are most likely indicative of a highly fractured medium or of a high pore fluid pressure.

4.4. Decrease in Stress Drops With Time Near the Trench

As we have discussed, the near-trench region appears distinct from the rest of the study area. Not only is it a region of lower stress drops, but we also observe throughout the postseismic period a decrease in stress drops, seismic moments, and sometimes corner frequencies with time within families of repeating earthquakes. We have established that neither transient embrittlement nor fault weakening can explain such behavior, as recurrence times also increase with time. An increase in attenuation could perhaps explain the apparent stress drop decrease, or more likely a combination of decreasing stress drops and increasing attenuation. However, even if attenuation plays a role in this trend, the underlying process that would cause attenuation to be low right after a large earthquake and to increase over time remains to be explained.

We propose that this change in stress drops, and possibly attenuation, could be linked to a change in normal stress likely resulting from an increase in pore fluid pressure during the period. Lengliné et al. (2014) found that, in the context of fluid injections, repeaters can have very similar corner frequencies but very different stress drops likely linked to rapid changes in pore fluid pressure. Cauchie et al. (2020) made similar observations in the same region at a different date, although in both cases there was no specific trend of stress drops with time. Other studies looking at non-repeaters have found a dependence of stress drops on pore fluid pressure in injection sites (Staszek et al., 2017) as well as in natural environments (Yoshida et al., 2017).

We propose that our observed stress drop decrease is due to an increase in pore fluid pressure linked to fault-valve behavior (Husen & Kissling, 2001; Sibson, 1990), as we explain in Figure 10. This would mean that before the mainshock, the subduction interface acted as a low-permeability zone, leaving fluid pressure to build up. The afterslip, by dilatancy effects or by breaking the seal, may have lowered pore fluid pressure. However, as afterslip decreased, slab fractures and the subduction interface were gradually resealed by precipitate-hosting fluid advection and diffusion, leading to a new increase in pore fluid pressure and a subsequent decrease in frictional strength and increase in attenuation. This behavior has been documented in subduction zones after both megathrust earthquakes (Husen & Kissling, 2001; Magee & Zoback, 1993) and SSEs (Nakajima & Uchida, 2018; Warren-Smith et al., 2019), and is visible in the geological record (Cerchiari et al., 2020). The decrease in stress drops that we are observing is therefore likely the last stage of this process, associated with fluid-pressure build up. This idea might be further supported by the fact that no repeating earthquake has been detected near the trench in the south in the year before the mainshock, and only two occur in the second half of the study period (Chalumeau et al., 2021). Meanwhile, down-dip of this region, two repeaters occur in the year before the mainshock, and repeaters continue to occur throughout the subsequent 440 days (Chalumeau et al., 2021). Additionally, the near-trench region saw little activity during the interseismic period compared to the postseismic period, even from regular earthquakes (Font et al., 2013; Soto-Cordero et al., 2020). It is therefore possible that most of the near-trench seismicity, repeating and not, emerged as a result of low pressure linked to the afterslip activity, and disappeared as afterslip slowed down and pressure increased again.

5. Conclusions

We computed the corner frequencies, seismic moments and stress drops of 341 small Mw 2–4 earthquakes along the Ecuadorian subduction zone in the aftermath of the Mw 7.8 2016 Pedernales earthquake. Stress drops were found to increase with magnitude, as well as with distance to the trench. When examining the variation of source properties within repeating earthquakes, we find that in most of the region they are spatially variable with no clear pattern of evolution, and likely influenced by local processes. Near the trench, however, earthquake stress drops systematically decrease over time. This may reflect changes in pore fluid pressure associated with the decay of the afterslip. Thus our work allows us to image changes in friction of the megathrust in space and time.

Appendix A

The rapid response team of the 2016 Pedernales earthquake:

Audrey Galve[1], Andreas Rietbrock[2], Alexandra Alvarado[3], Colton Lynner[4], Stephen Hernandez[3], Susan Beck[4], Yvonne Font[1], Mariah C. Hoskins[5], Sergio Leon-Rios[2], Anne Meltzer[5], Frédérique Rolandone[6], Jean-Mathieu Nocquet[1], Marc Régnier[1], Mario Ruiz[3], Lillian Soto Cordero[5], Sandro Vaca[3], Monica Segovia[3]

[1]Université Côte d'Azur, IRD, CRNS, Observatoire de la Côte d'Azur, Géoazur, UMR, Valbonne, France

[2]Geophysical Institute (GPI), Karlsruhe Institute of Technology, Karlsruhe, Germany

[3]Instituto Geofísico at the Escuela Politécnica Nacional, Quito, Ecuador

[4]Department of Geosciences, University of Arizona, Tucson, AZ, USA

[5]Department of Earth and Environmental Sciences, Lehigh University, Bethlehem, PA, USA

[6]Sorbonne Université, CNRS-INSU, Institut des Sciences de la Terre Paris, ISTeP, UMR, Paris, France

Data Availability Statement

The original earthquake catalog is available from Agurto-Detzel et al. (2019) supplementary material, and original waveforms from the 8G, EC, XE, and IU networks are available from the IRIS depository. Generic Mapping Tools v5.2.1 (Wessel et al., 2013) and Python 2.6 (https://www.python.org) were used to make the maps and figures.

Acknowledgments

We would like to thank our editor and reviewers for their help in improving our manuscript. This work was supported by the REMAKE project (ANR-15-CE04-0004) and the UCA/JEDI project (ANR-15-IDEX-01). The deployment of the geophysical network for post-seismic data acquisition was possible thanks to the logistics and support of an international team including the Instituto Geofísico de la Escuela Politécnica Nacional (IG-EPN) of Quito, Ecuador, the French National Research Institute for Sustainable Development (IRD), the National Institute for Earth Sciences and Astronomy of CNRS, the University of Liverpool UK, the National Science Foundation NSF RAPID Program (Award EAR-1642498) and the NSF Geophysics Program (Awards EAR-1723042 and EAR-1723065). This work is a contribution of the International Joint Laboratory "Earthquakes and Volcanoes in the Northern Andes" (LMI SVAN).

References

Abercrombie, R. E. (1995). Earthquake source scaling relationships from 1 to 5 Ml using seismograms recorded at 2.5 km depth. *Journal of Geophysical Research*, *100*(B12), 24015–24036. https://doi.org/10.1029/95jb02397

Abercrombie, R. E. (2014). Stress drops of repeating earthquakes on the San Andreas Fault at Parkfield. *Geophysical Research Letters*, *41*(24), 8784–8791. https://doi.org/10.1002/2014GL062079.Received

Abercrombie, R. E. (2015). Investigating uncertainties in empirical Green's function analysis of earthquake source parameters. *Journal of Geophysical Research: Solid Earth*, *120*(6), 4263–4277. https://doi.org/10.1002/2015JB011984.Received

Abercrombie, R. E. (2021). Resolution and uncertainties in estimates of earthquake stress drop and energy release. *Philosophical Transactions Royal Society*, *379*(2196), 20200131. https://doi.org/10.1098/rsta.2020.0131

Abercrombie, R. E., Bannister, S., Ristau, J., & Doser, D. (2017). Variability of earthquake stress drop in a subduction setting, the Hikurangi Margin, New Zealand. *Geophysical Journal International*, *208*(1), 306–320. https://doi.org/10.1093/gji/ggw393

Abercrombie, R. E., Chen, X., & Zhang, J. (2012). Repeating earthquakes with remarkably repeatable ruptures on the San Andreas Fault at Parkfield. *Geophysical Research Letters*, *47*(47), 1–15. https://doi.org/10.1029/2020GL089820

Agurto-detzel, H., Bianchi, M., Prieto, G. A., & Assumpção, M. (2017). Earthquake source properties of a shallow induced seismic sequence in SE Brazil. *Journal of Geophysical Research: Solid Earth*, *122*(4), 2784–2797. https://doi.org/10.1002/2016JB013623

Agurto-Detzel, H., Font, Y., Charvis, P., Régnier, M., Rietbrock, A., Ambrois, D., et al. (2019). Ridge subduction and afterslip control aftershock distribution of the 2016 Mw 7.8 Ecuador earthquake. *Earth and Planetary Science Letters*, *520*, 63–76. https://doi.org/10.1016/j.epsl.2019.05.029

Aki, K. (1966). Generation and propagation of G waves from the Niigata earthquake of June 16, 1964. Part 2. Estimation of earthquake moment, released energy and stress-strain drop from G wave spectrum. *Bulletin of the Earthquake Research Institute*, *44*, 73–88.

Aki, K. (1967). Scaling law of seismic spectrum. *Journal of Geophysical Research*, *72*(4), 1217–1231. https://doi.org/10.1029/JZ072i004p01217

Allmann, B. P., & Shearer, P. M. (2007). Spatial and temporal stress drop variations in small earthquakes near Parkfield, California. *Journal of Geophysical Research*, *112*, B04305. https://doi.org/10.1029/2006JB004395

Allmann, B. P., & Shearer, P. M. (2009). Global variations of stress drop for moderate to large earthquakes. *Journal of Geophysical Research*, *114*, 1–22. https://doi.org/10.1029/2008JB005821

Alvarado, A., Ruiz, M., Mothes, P. A., Yepes, H., Segovia, M., Vaca, M., et al. (2018). Seismic, volcanic, and geodetic networks in Ecuador: Building capacity for monitoring and research. *Seismological Research Letters*, *89*(2A), 432–439. https://doi.org/10.1785/0220170229

Baltay, A. S., Hanks, T. C., & Beroza, G. C. (2013). Stable stress-drop measurements and their variability: Implications for ground-motion prediction. *Bulletin of the Seismological Society of America*, *103*(1), 211–222. https://doi.org/10.1785/0120120161

Beeler, N. M., Lockner, D. L., & Hickman, S. H. (2001). A simple stick-slip and creep-slip model for repeating earthquakes and its implication for microearthquakes at Parkfield. *Bulletin of the Seismological Society of America*, *91*(6), 1797–1804. https://doi.org/10.1785/0120000096

Bilek, S. L. (2007). Using earthquake source durations along the Sumatra—Andaman subduction system to examine fault-zone variations. *Bulletin of the Seismological Society of America*, *97*(1), 62–70. https://doi.org/10.1785/0120050622

Bilek, S. L., & Lay, T. (2002). Tsunami earthquakes possibly widespread manifestations of frictional conditional stability. *Geophysical Research Letters*, *29*(14), 18-1–18-4. https://doi.org/10.1029/2002gl015215

Bindi, D., Spallarossa, D., Picozzi, M., & Morasca, P. (2020). Reliability of source parameters for small events in central Italy: Insights from spectral decomposition analysis applied to both synthetic and real data. *Bulletin of the Seismological Society of America*, *110*(6), 3139–3157. https://doi.org/10.1785/0120200126

Boatwright, J. (1980). A spectral theory for circular seismic sources; simple estimates of source dimension, dynamic stress drop, and radiated seismic energy. *Bulletin of the Seismological Society of America*, *70*(1).

Boore, D. M., & Boatwright, J. (1984). Average body-wave radiation coefficients. *Bulletin of the Seismological Society of America*, *74*(5), 1615–1621. https://doi.org/10.1785/bssa0740051615

Boyd, O. S., Mcnamara, D. E., Hartzell, S., & Choy, G. (2017). Influence of lithostatic stress on earthquake stress drops in North America. *Bulletin of the Seismological Society of America*, *107*(2), 856–868. https://doi.org/10.1785/0120160219

Brune, J. N. (1970). Tectonic stress and the spectra of seismic shear waves from earthquakes. *Journal of Geophysical Research*, *75*(26), 4997–5009. https://doi.org/10.1029/jb075i026p04997

Cauchie, L., Lengliné, O., & Schmittbuhl, J. (2020). Seismic asperity size evolution during fluid injection: Case study of the 1993 Soultz-sous-Forêts injection. *Geophysical Journal International*, *221*(2), 968–980. https://doi.org/10.1093/gji/ggaa051

Cerchiari, A., Remitti, F., Mittempergher, S., Festa, A., Lugli, F., & Cipriani, A. (2020). Cyclical variations of fluid sources and stress state in a shallow megathrust-zone mélange. *Journal of the Geological Society*, *177*(3), 647–659. https://doi.org/10.1144/jgs2019-072

Chalumeau, C., Agurto-detzel, H., De Barros, L., Charvis, P., Galve, A., Rietbrock, A., et al. (2021). Repeating earthquakes at the edge of the afterslip of the 2016 Ecuadorian M_w 7.8 Pedernales earthquake. *Journal of Geophysical Research: Solid Earth*, *126*(5), e2021JB021746. https://doi.org/10.1029/2021JB021746

Chaves, E. J., Schwartz, S. Y., & Abercrombie, R. E. (2020). Repeating earthquakes record fault weakening and healing in areas of megathrust postseismic slip. *Science Advances*, *6*(32). https://doi.org/10.1126/sciadv.aaz9317

Chen, K. H., Bürgmann, R., Nadeau, R. M., Chen, T., & Lapusta, N. (2010). Postseismic variations in seismic moment and recurrence interval of repeating earthquakes. *Earth and Planetary Science Letters*, *299*(1–2), 118–125. https://doi.org/10.1016/j.epsl.2010.08.027

Chen, T., & Lapusta, N. (2009). Scaling of small repeating earthquakes explained by interaction of seismic and aseismic slip in a rate and state fault model. *Journal of Geophysical Research*, *114*(1), 1–12. https://doi.org/10.1029/2008JB005749

Chen, X., & Shearer, P. M. (2011). Comprehensive analysis of earthquake source spectra and swarms in the Salton Trough, California. *Journal of Geophysical Research*, *116*(B9), B09309. https://doi.org/10.1029/2011JB008263

Chen, X., & Shearer, P. M. (2013). California foreshock sequences suggest aseismic triggering process. *Geophysical Research Letters*, *40*(11), 2602–2607. https://doi.org/10.1002/grl.50444

Chlieh, M., Mothes, P. A., Nocquet, J.-M., Jarrín, P., Charvis, P., Cisneros, D., et al. (2014). Distribution of discrete seismic asperities and aseismic slip along the Ecuadorian megathrust. *Earth and Planetary Science Letters*, *400*, 292–301. https://doi.org/10.1016/j.epsl.2014.05.027

Collot, J.-Y., Marcaillou, B., Sage, F., Michaud, F., Agudelo, W., Charvis, P., et al. (2004). Are rupture zone limits of great subduction earthquakes controlled by upper plate structures? Evidence from multichannel seismic reflection data acquired across the northern Ecuador—Southwest Colombia margin. *Journal of Geophysical Research*, *109*(11), 1–14. https://doi.org/10.1029/2004JB003060

Drouet, S., Bouin, M.-P., & Cotton, F. (2011). New moment magnitude scale, evidence of stress drop magnitude scaling and stochastic ground motion model for the French West Indies. *Geophysical Journal International*, *187*(3), 1625–1644. https://doi.org/10.1111/j.1365-246X.2011.05219.x

Ellsworth, W. L. (1995). Characteristic earthquakes and long-term earthquake forecasts: Implications of central California seismicity. In *Urban disaster mitigation: The role of engineering and technology*.

Eshelby, J. D. (1957). The determination of the elastic field of an ellipsoidal inclusion, and related problems. *Proceedings of the Royal Society of London*, 376–396.

Font, Y., Segovia, M., Vaca, S., & Theunissen, T. (2013). Seismicity patterns along the Ecuadorian subduction zone: New constraints from earthquake location in a 3-D a priori velocity model. *Geophysical Journal International*, *193*(1), 263–286. https://doi.org/10.1093/gji/ggs083

Gailler, A., Charvis, P., & Flueh, E. R. (2007). Segmentation of the Nazca and South American plates along the Ecuador subduction zone from wide angle seismic profiles. *Earth and Planetary Science Letters*, *260*(3–4), 444–464. https://doi.org/10.1016/j.epsl.2007.05.045

Goertz-Allmann, B. P., Goertz, A., & Wiemer, S. (2011). Stress drop variations of induced earthquakes at the Basel geothermal site. *Geophysical Research Letters*, *38*(9), L09308. https://doi.org/10.1029/2011GL047498

Graindorge, D., Calahorrano, A., Charvis, P., Collot, J., & Bethoux, N. (2004). Deep structures of the Ecuador convergent margin and the Carnegie Ridge, possible consequence on great earthquakes recurrence interval. *Geophysical Research Letters*, *31*(4), L04603. https://doi.org/10.1029/2003GL018803

Hanks, T. C., & Kanamori, H. (1979). A moment magnitude scale. *Journal of Geophysical Researc*h, *84*(B5), 2348–2350. https://doi.org/10.1029/JB084iB05p02348

Hardebeck, J. L., & Aron, A. (2009). Earthquake stress drops and inferred fault strength on the Hayward Fault, East San Francisco Bay, California. *Bulletin of the Seismological Society of America*, *99*(3), 1801–1814. https://doi.org/10.1785/0120080242

Hatakeyama, N., Uchida, N., Matsuzawa, T., & Nakamura, W. (2017). Emergence and disappearance of interplate repeating earthquakes following the 2011 M9.0 Tohoku-oki earthquake: Slip behavior transition between seismic and aseismic depending on the loading rate. *Journal of Geophysical Research: Solid Earth*, *122*(7), 5160–5180. https://doi.org/10.1002/2016JB013914

Hayes, G. P., Wald, D. J., & Johnson, R. L. (2012). Slab1.0: A three-dimensional model of global subduction zone geometries. *Journal of Geophysical Research*, *117*(B1), B01302. https://doi.org/10.1029/2011JB008524

Hough, S. E. (1997). Empirical Green's function analysis: Taking the next step. *Journal of Geophysical Researc*h, *102*(B3), 5369–5384. https://doi.org/10.1029/96jb03488

Huang, Y., Ellsworth, W. L., & Beroza, G. C. (2017). Stress drops of induced and tectonic earthquakes in the central United States are indistinguishable. *Science Advances*, *3*(8), e1700772. https://doi.org/10.1126/sciadv.1700772

Husen, S., & Kissling, E. (2001). Postseismic fluid flow after the large subduction earthquake of Antofagasta, Chile. *Geology*, *29*(9), 847–850. https://doi.org/10.1130/0091-7613(2001)029<0847:pffatl>2.0.co;2

Ide, S., Beroza, G. C., Prejean, S. G., & Ellsworth, W. L. (2003). Apparent break in earthquake scaling due to path and site effects on deep borehole recordings. *Journal of Geophysical Research*, *108*, 2271. https://doi.org/10.1029/2001JB001617

Kanamori, H., & McNally, K. (1982). Variable rupture mode of the subduction zone along the Ecuador-Colombia coast. *Bulletin of the Seismological Society of America*, *72*(4), 1241–1253.

Kaneko, Y., & Shearer, P. M. (2014). Seismic source spectra and estimated stress drop derived from cohesive-zone models of circular subshear rupture. *Geophysical Journal International*, *197*(2), 1002–1015. https://doi.org/10.1093/gji/ggu030

Kaneko, Y., & Shearer, P. M. (2015). Variability of seismic source spectra, estimated stress drop, and radiated energy, derived from cohesive-zonemodels of symmetrical and asymmetrical circular and elliptical ruptures. *Journal of Geophysical Research: Solid Earth*, *120*(2), 1053–1079. https://doi.org/10.1002/2014JB011642.Received

Kelleher, J. A. (1972). Rupture zones of large South American earthquakes and some predictions. *Journal of Geophysical Research*, *77*(11), 2087–2103. https://doi.org/10.1029/jb077i011p02087

Kelly, C. M., Rietbrock, A., Faulkner, D. R., & Nadeau, R. M. (2013). Temporal changes in attenuation associated with the 2004 M6.0 Parkfield earthquake. *Journal of Geophysical Research: Solid Earth*, *118*(2), 630–645. https://doi.org/10.1002/jgrb.50088

Koch, C. D., Lynner, C., Delph, J., Beck, S. L., Meltzer, A., Font, Y., et al. (2020). Structure of the Ecuadorian forearc from the joint inversion of receiver functions and ambient noise surface waves. *Geophysical Journal International*, *222*(3), 1671–1685. https://doi.org/10.1093/gji/ggaa237

Kwiatek, G., Bulut, F., Bohnhoff, M., & Dresen, G. (2014). High-resolution analysis of seismicity induced at Berlín geothermal. *Geothermics*, *52*, 98–111. https://doi.org/10.1016/j.geothermics.2013.09.008

Lay, T., & Bilek, S. L. (2007). Anomalous earthquake ruptures at shallow depths on subduction zone megathrusts. In T. H. Dixon & C. Moore (Eds.), *The seismogenic zone of subduction thrust faults* (pp. 476–511). Columbia University Press.

Lay, T., Kanamori, H., Ammon, C. J., Koper, K. D., Hutko, A. R., Ye, L., et al. (2012). Depth-varying rupture properties of subduction zone megathrust faults. *Journal of Geophysical Research*, *117*(B4), B04311. https://doi.org/10.1029/2011JB009133

Lengliné, O., Lamourette, L., Vivin, L., Cuenot, N., & Schmittbuhl, J. (2014). Fluid-induced earthquakes with variable stress drop. *Journal of Geophysical Research: Solid Earth*, *119*(12), 8900–8913. https://doi.org/10.1002/2014JB011282.Received

León-ríos, S., Bie, L., Agurto-detzel, H., Rietbrock, A., Galve, A., Alvarado, A., et al. (2021). 3D local earthquake tomography of the Ecuadorian margin in the source area of the 2016 Mw 7.8 Pedernales earthquake. *Journal of Geophysical Research: Solid Earth*, *126*(3), e2020JB020701. https://doi.org/10.1029/2020JB020701

Lin, Y., & Lapusta, N. (2018). Microseismicity simulated on Asperity-Like Fault Patches: On scaling of seismic moment with duration and seismological estimates of stress drops. *Geophysical Research Letters*, *45*(16), 8145–8155. https://doi.org/10.1029/2018GL078650

Lomax, A., Virieux, J., Volant, P., & Berge-thierry, C. (2000). Probabilistic earthquake location in 3D and layered models.

Lynner, C., Koch, C. D., Beck, S. L., Meltzer, A., Soto-Cordero, L., Hoskins, M. C., et al. (2020). Upper-plate structure in Ecuador coincident with the subduction of the Carnegie Ridge and the southern extent of large mega-thrust earthquakes. *Geophysical Journal International*, *220*(3), 1965–1977. https://doi.org/10.1093/gji/ggz558

Magee, M. E., & Zoback, M. D. (1993). Evidence for a weak interplate thrust fault along the northern Japan subduction zone and implications for the mechanics of thrust faulting and fluid expulsion. *Geology*, *21*(9), 809–812. https://doi.org/10.1130/0091-7613(1993)021<0809:efawit>2.3.co;2

Marcaillou, B., Collot, J., Ribodetti, A., D'Acremont, E., Mahamat, A., & Alvarado, A. (2016). Seamount subduction at the North-Ecuadorian convergent margin: Effects on structures, inter-seismic coupling and seismogenesis. *Earth and Planetary Science Letters*, *433*, 146–158. https://doi.org/10.1016/j.epsl.2015.10.043

Meltzer, A., Beck, S. L., Ruiz, M., Soto-cordero, L., Stachnik, J. C., Lynner, C., et al. (2019). The 2016 Mw 7.8 Pedernales, Ecuador, earthquake: Rapid response deployment. *Seismological Research Letters*, *90*(3), 1346–1354. https://doi.org/10.1785/0220180364

Mendoza, C., & Dewey, J. W. (1984). Seismicity associated with the great Colombia-Ecuador earthquakes of 1942, 1958, and 1979: Implications for barrier models of earthquake rupture. *Bulletin of the Earthquake Research Institute*, *74*(2), 577–593.

Michaud, F., Witt, C., & Royer, J. Y. (2009). Influence of the subduction of the Carnegie volcanic ridge on Ecuadorian geology: Reality and fiction. *Geological Society of America*, *204*. https://doi.org/10.1130/2009.1204

Nadeau, R. M., & Johnson, L. R. (1998). Seismological studies at Parkfield VI: Moment release rates and estimates of source parameters for small repeating earthquakes. *Bulletin of the Seismological Society of America*, *88*(3), 790–814. https://doi.org/10.1785/bssa0880030790

Nakai, J. S., Sheehan, A. F., Abercrombie, R. E., & Eberhart-Phillips, D. (2021). Near trench 3D seismic attenuation offshore Northern Hikurangi subduction margin, North Island, New Zealand. *Journal of Geophysical Research: Solid Earth*, *126*(3), e2020JB020810. https://doi.org/10.1029/2020JB020810

Nakajima, J., & Uchida, N. (2018). Repeated drainage from megathrusts during episodic slow slip. *Nature Geoscience*, *11*(5), 351–356. https://doi.org/10.1038/s41561-018-0090-z

Nocquet, J.-M., Jarrín, P., Vallée, M., Mothes, P. A., Grandin, R., Rolandone, F., et al. (2017). Supercycle at the Ecuadorian subduction zone revealed after the 2016 Pedernales earthquake. *Nature Geoscience*, *10*(2), 145–149. https://doi.org/10.1038/ngeo2864

Nocquet, J.-M., Villegas-Lanza, J. C., Chlieh, M., Mothes, P. A., Rolandone, F., Jarrín, P., et al. (2014). Motion of continental slivers and creeping subduction in the northern Andes. *Nature Geoscience*, *7*(4), 287–291. https://doi.org/10.1038/NGEO2099

Oth, A. (2013). On the characteristics of earthquake stress release variations in Japan. *Earth and Planetary Science Letters*, *377*(378), 132–141. https://doi.org/10.1016/j.epsl.2013.06.037

Oth, A., Bindi, D., Parolai, S., & Di Giacomo, D. (2010). Earthquake scaling characteristics and the scale-(in) dependence of seismic energy-to-moment ratio: Insights from KiK-net data in Japan. *Geophysical Research Letters*, *37*(19), L19304. https://doi.org/10.1029/2010GL044572

Passelègue, F. X., Almakari, M., Dublanchet, P., Barras, F., Fortin, J., & Violay, M. (2020). Initial effective stress controls the nature of earthquakes. *Nature Communications*, *11*, 1–8. https://doi.org/10.1038/s41467-020-18937-0

Peng, Z., Vidale, J. E., Marone, C., & Rubin, A. M. (2005). Systematic variations in recurrence interval and moment of repeating aftershocks. *Geophysical Research Letters*, *32*, 3–6. https://doi.org/10.1029/2005GL022626

Prieto, G. A., Parker, R. L., Thomson, D. J., Vernon, F. L., & Graham, R. L. (2007). Reducing the bias of multitaper spectrum estimates. *Geophysical Journal International*, *171*(3), 1269–1281. https://doi.org/10.1111/j.1365-246X.2007.03592.x

Prieto, G. A., Parker, R. L., & Vernon, F. L. (2009). A Fortran 90 library for multitaper spectrum analysis. *Computers & Geosciences*, *35*(8), 1701–1710. https://doi.org/10.1016/j.cageo.2008.06.007

Rolandone, F., Nocquet, J.-M., Mothes, P. A., Jarrín, P., Vallée, M., Cubas, N., et al. (2018). Areas prone to slow slip events impede earthquake rupture propagation and promote afterslip. *Science Advances*, *4*, 2–10. https://doi.org/10.1126/sciadv.aao6596

Soto-Cordero, L., Meltzer, A., Bergman, E., Hoskins, M. C., Stachnik, J. C., Agurto-detzel, H., et al. (2020). Structural control on megathrust rupture and slip behavior: Insights from the 2016 Mw 7.8 Pedernales Ecuador earthquake. *Journal of Geophysical Research: Solid Earth*, *125*(2), 1–28. https://doi.org/10.1029/2019JB018001

Sallarès, V., Charvis, P., Flueh, E. R., & Bialas, J. (2005). Seismic structure of the Carnegie ridge and the nature of the Galapagos hotspot. *Geophysical Journal International*, *161*(3), 763–788. https://doi.org/10.1111/j.1365-246X.2005.02592.x

Scholz, C. H. (1998). Earthquakes and friction laws. *Nature*, *391*(6662), 37–42. https://doi.org/10.1038/34097

Shearer, P. M. (2009). *Introduction to Seismology* (2nd ed.). Cambridge University Press.

Shearer, P. M., Abercrombie, R. E., Trugman, D. T., & Wang, W. (2019). Comparing EGF methods for estimating corner frequency and stress drop from P wave spectra. *Journal of Geophysical Research: Solid Earth*, *124*(4), 3966–3986. https://doi.org/10.1029/2018JB016957

Shearer, P. M., Prieto, G. A., & Hauksson, E. (2006). Comprehensive analysis of earthquake source spectra in southern California. *Journal of Geophysical Research*, *111*(B6), B06303. https://doi.org/10.1029/2005JB003979

Sibson, R. H. (1990). Conditions for fault-valve behaviour. *Geological Society Special Publication*, *54*(1), 15–28. https://doi.org/10.1144/gsl.sp.1990.054.01.02

Staszek, M., Orlecka-Sikora, B., Leptokaropoulos, K., Kwiatek, G., & Martinez-Garzon, P. (2017). Temporal static stress drop variations due to injection activity at the Geysers geothermal field, California. *Geophysical Research Letters*, *44*(14), 7168–7176. https://doi.org/10.1002/2017GL073929

Tolga Şen, A., Cesca, S., Lange, D., Dahm, T., Tilmann, F., & Heimann, S. (2015). Systematic changes of earthquake rupture with depth: A case study from the 2010 Mw 8.8 Maule, Chile, earthquake aftershock sequence. *Bulletin of the Seismological Society of America*, *105*(5), 2468–2479. https://doi.org/10.1785/0120140123

Tsang, L. L. H., Vergnolle, M., Twardzik, C., Sladen, A., Nocquet, J., Rolandone, F., et al. (2019). Imaging rapid early afterslip of the 2016 Pedernales earthquake, Ecuador. *Earth and Planetary Science Letters*, *524*, 115724. https://doi.org/10.1016/j.epsl.2019.115724

Uchida, N., Shimamura, K., Matsuzawa, T., & Okada, T. (2015). Postseismic response of repeating earthquakes around the 2011 Tohoku-oki earthquake: Moment increases due to the fast loading rate. *Journal of Geophysical Research: Solid Earth*, *120*(1), 259–274. https://doi.org/10.1002/2013JB010933.Received

Uchide, T., Shearer, P. M., & Imanishi, K. (2014). Stress drop variations among small earthquakes before the 2011 Tohoku-oki, Japan, earthquake and implications for the main shock. *Journal of Geophysical Research: Solid Earth*, *119*(9), 7164–7174. https://doi.org/10.1002/2014JB010943.Received

Vaca, S., Vallée, M., Nocquet, J.-M., Battaglia, J., & Régnier, M. (2018). Recurrent slow slip events as a barrier to the northward rupture propagation of the 2016 Pedernales earthquake (Central Ecuador). *Tectonophysics*, *724–725*, 80–92. https://doi.org/10.1016/j.tecto.2017.12.012

Vidale, J. E., Ellsworth, W. L., Cole, A., & Marone, C. (1994). Variations in rupture process with recurrence interval in a repeated small earthquake. *Nature Letters*, *368*(6472), 624–626. https://doi.org/10.1038/368624a0

Viegas, G., Abercrombie, R. E., & Kim, W. Y. (2010). The 2002 M5 Au Sable Forks, NY, earthquake sequence: Source scaling relationships and energy budget. *Journal of Geophysical Research*, *115*(B7), B07310. https://doi.org/10.1029/2009JB006799

Waldhauser, F., & Ellsworth, W. L. (2000). A double-difference earthquake location algorithm: Method and application to the northern Hayward Fault, California. *Bulletin of the Seismological Society of America*, *90*(6), 1353–1368. https://doi.org/10.1785/0120000006

Warren-Smith, E., Fry, B., Wallace, L. M., Chon, E., Henrys, S., Sheehan, A. F., et al. (2019). Episodic stress and fluid pressure cycling in subducting oceanic crust during slow slip. *Nature Geoscience*, *12*, 475–482. https://doi.org/10.1038/s41561-019-0367-x

Wessel, P., Smith, W. H. F., Scharroo, R., Luis, J., & Wobbe, F. (2013). Generic mapping tools: Improved version released. *Eos*, *94*(45), 409–410. https://doi.org/10.1002/2013eo450001

Yamada, T., Duan, M., & Kawahara, J. (2021). Spatio-temporal characteristics of frictional properties on the subducting Pacific Plate off the east of Tohoku district, Japan estimated from stress drops of small earthquakes. *Earth Planets and Space*, *73*(18), 18. https://doi.org/10.1186/s40623-020-01326-8

Ye, L., Kanamori, H., Avouac, J., Li, L., Fai Cheung, K., Lay, T., et al. (2016). The 16 April 2016, Mw 7.8 (Ms 7.5) Ecuador earthquake: A quasi-repeat of the 1942 Ms7.5 earthquake and partial re-rupture of the 1906 Ms8.6 Colombia–Ecuador earthquake. *Earth and Planetary Science Letters*, *454*, 248–258. https://doi.org/10.1016/j.epsl.2016.09.006

Yoshida, K., Saito, T., Urata, Y., Asano, Y., & Hasegawa, A. (2017). Temporal changes in stress drop, frictional strength, and earthquake size distribution in the 2011 Yamagata-Fukushima, NE Japan, earthquake swarm, caused by fluid migration. *Journal of Geophysical Research: Solid Earth*, *122*(12), 10379–10397. https://doi.org/10.1002/2017JB014334

Yoshimoto, M., Kumagai, H., Acero, W., Ponce, G., Vásconez, F., Arrais, S., et al. (2017). Depth-dependent rupture mode along the Ecuador-Colombia subduction zone. *Geophysical Research Letters*, *44*(5), 2203–2210. https://doi.org/10.1002/2016GL071929